

# The Swelling Behavior of Clay-Sulfate Rocks

by

Ann S. Chen

B.A., Chemistry and Economics  
Wellesley College  
(1996)

Submitted to the Department of Civil and Environmental Engineering  
in Partial Fulfillment of the Requirements for the Degree of  
Master of Science in Civil and Environmental Engineering

at the

Massachusetts Institute of Technology

June 1998

© 1998 Massachusetts Institute of Technology  
All Rights Reserved

Signature of Author \_\_\_\_\_

Department of Civil and Environmental Engineering  
May 18, 1998

Certified by \_\_\_\_\_

Professor Herbert H. Einstein  
Professor of Civil and Environmental Engineering  
Thesis Co-Supervisor

Certified by \_\_\_\_\_

Dr. John T. Germaine  
Principal Research Associate in Civil and Environmental Engineering  
Thesis Co-Supervisor

Accepted by \_\_\_\_\_

Professor Joseph M. Sussman  
Chairman, Department Committee on Graduate Students

JUN 02 1998

LIBRARIES

Eng.



# The Swelling Behavior of Clay-Sulfate Rocks

by  
Ann S. Chen

Submitted to the  
Department of Civil and Environmental Engineering  
on May 18, 1998 in partial fulfillment of the  
requirements for the Degree of Master of Science in  
Civil and Environmental Engineering

## Abstract

Clay-sulfate rocks are often encountered in engineering projects such as underground construction and waste repositories. The unique combination of clay swelling and chemical transformation of anhydrite into gypsum results in a swelling behavior that cannot be explained using conventional rock mechanics. The goals of this study are: 1) to investigate the strength characteristics of reconstituted clay-sulfate rocks and 2) to assess the influence of shearing on the gypsification of anhydrite.

The specimens used in this testing program consist of 85% anhydrite and 15% clay and were hydrostatically formed at 100 MPa. Undrained and drained triaxial compression tests were performed on these specimens. The results showed that these clay-sulfate rocks have a normalized undrained shear strength of 0.504-0.792 and a friction angle  $\alpha$  of 17.2°. The normalized undrained strength of this predominantly anhydritic rock is low compared to natural shales of the same OCR. Depending on the shearing rate, specimens exhibited either ductile or brittle failure. Specimens sheared at faster rates failed brittlely, while those sheared at slower rates bulged at failure.

Water content analysis was used to determine gypsification levels and involved isolating gypsum water from pore and adsorbed water. Due to cracking of gypsum shells caused by shearing, sheared specimens showed higher gypsification levels than unsheared specimens. In specimens that bulged, gypsification levels were relatively uniform throughout the specimen, with slightly higher levels at the boundaries. Specimens that failed with shear planes showed generally higher gypsification levels than bulged specimens. The brittle specimens also showed enhanced gypsification in the shear plane. This increase in gypsification is due to dilation, which draws water into the shear zone and allows more gypsification to occur. Like the bulged specimens, specimens with shear planes also had slightly higher levels of gypsum water at the boundaries.

Thesis Co-Supervisor: Professor Herbert H. Einstein  
Title: Professor of Civil and Environmental Engineering

Thesis Co-Supervisor: Dr. John T. Germaine  
Title: Principal Research Associate in Civil and Environmental Engineering



*Special thanks to --*

*Professor Herbert H. Einstein, for your unyielding guidance and support in my  
research*

*Dr. John T. Germaine, for your ingenuity and patience with my research (and me)*

*Dr. Rolf Nüesch, for your encouragement and expertise*

*The Lab Rats –Lana Aref, Greg Da Re, Erin Force, Laurent Levy, Catalina  
Marulanda, Marika Santagata, Joe Sinfield, Kurt Sjoblom, Guoping Zhang --  
for smiles, laughs, and support*

*My parents, for giving me the opportunity to do anything I can dream of*



# Table of Contents

<b>1</b>	<b>INTRODUCTION.....</b>	<b>13</b>
1.1	NATURE OF CLAY-SULFATE ROCKS.....	13
1.1.1	<i>Origin.....</i>	13
1.1.2	<i>Problems with clay-sulfate rocks.....</i>	13
1.2	CLAY ROCK BEHAVIOR.....	14
1.2.1	<i>Clay Swelling Mechanism: Adsorption.....</i>	14
1.2.2	<i>Strength of Shales.....</i>	15
1.3	SULFATE BEHAVIOR.....	18
1.3.1	<i>Anhydrite Swelling Mechanism: Gypsification.....</i>	18
1.4	CLAY-SULFATE BEHAVIOR.....	19
1.4.1	<i>Clay-Sulfate Swelling.....</i>	19
1.4.2	<i>Deformational Behavior of Clay-Sulfate Rocks.....</i>	21
1.5	APPLICATIONS OF CLAY-SULFATE ROCKS.....	22
1.6	THE TESTING PROGRAM.....	23
<b>2</b>	<b>MATERIALS AND PROCEDURES.....</b>	<b>37</b>
2.1	NATURE OF TESTING MATERIAL.....	37
2.1.1	<i>Mineralogy and Sample Preparation Method.....</i>	37
2.2	TRIAXIAL TESTING EQUIPMENT.....	38
2.2.1	<i>The Triaxial Cell and Load Frame.....</i>	38
2.2.2	<i>Pressure-Volume Controllers.....</i>	41
2.2.3	<i>Computer Control.....</i>	43
2.3	SPECIMEN SETUP.....	45
2.4	TRIAXIAL TESTING PROCEDURES.....	47
2.5	GYSIFICATION ANALYSIS.....	50
2.5.1	<i>Pore Water.....</i>	50
2.5.2	<i>Adsorbed Water.....</i>	50
2.5.3	<i>Gypsum Water.....</i>	51
<b>3</b>	<b>DATA ANALYSIS.....</b>	<b>53</b>
3.1	TRIAXIAL TEST RESULTS.....	53
3.1.1	<i>Stress Paths.....</i>	53
3.2	SHEAR STRENGTH.....	57
3.2.1	<i>Stress-Strain Curves.....</i>	58
3.2.2	<i>B-values.....</i>	61
3.2.3	<i>Modes of Failure.....</i>	62
3.3	GYSIFICATION ANALYSIS.....	65
3.3.1	<i>Water Distribution.....</i>	66
3.3.2	<i>Effectiveness of <math>P_2O_5</math>.....</i>	66
3.3.3	<i>Adsorption and Gypsification Contours.....</i>	69
<b>4</b>	<b>CONCLUSION.....</b>	<b>75</b>
<b>5</b>	<b>REFERENCES.....</b>	<b>79</b>





## Table of Figures

Figure 1.1 Sheet structures for several common clay minerals .....	25
Figure 1.2 Peak friction angle as a function of porosity for different shales .....	26
Figure 1.3 Peak friction angle as a function of plasticity for different shales.....	27
Figure 1.4 Peak friction angle versus clay content for different shales.....	28
Figure 1.5 Peak friction angle versus illite content for different shales .....	29
Figure 1.6 Unconfined compressive strength versus illite content for different shales.....	30
Figure 1.7 Normalized undrained shear strength as a function of OCR for different shales .....	31
Figure 1.8 Maximum apparent pre-consolidation stress as a function of illite content for different shales .....	32
Figure 1.9 Maximum apparent pre-consolidation stress obtained from one-dimensional consolidation tests as a function of CaCO <sub>3</sub> for Pierre shale.....	33
Figure 1.10 Swelling stress versus clay content at 600 days of testing.....	34
Figure 1.11 Time-dependent swelling of shale, anhydrite, and shaley anhydrite rock.....	35
Figure 1.12 Stepwise swelling stress increase over time for clay-sulfate rock specimens .....	36
Figure 2.1 Triaxial chamber .....	38
Figure 2.2 Triaxial chamber in loading frame.....	39
Figure 2.3 Load transfer device.....	40
Figure 2.4 Load cell setup.....	41
Figure 2.5 Pressure-volume controller .....	42
Figure 2.6 Schematic diagram of triaxial setup and data acquisition system .....	43
Figure 2.7 Closed loop feedback control .....	44
Figure 2.8 Specimen and accessories.....	45
Figure 2.9 Sequence of water content analysis.....	49
Figure 3.1 Effective and total stress paths for undrained shear tests.....	55
Figure 3.2 Effective and total stress paths for drained shear tests .....	55
Figure 3.3 Pore pressure development during undrained shear .....	56
Figure 3.4 Stress states at failure .....	57
Figure 3.5 Stress-strain curves of undrained shear tests performed under different consolidation stresses.....	59
Figure 3.6 Stress-strain curves for undrained shear tests sheared at different rates .....	60
Figure 3.7 Ductile failure with corresponding stress-strain curve .....	64
Figure 3.8 Brittle failure with corresponding stress-strain curve.....	64
Figure 3.9 Water distribution contours throughout specimen after back pressure saturation .....	68
Figure 3.10 Sample taken from bulged specimen.....	69
Figure 3.11 Gypsification and adsorption contour for a bulging specimen.....	70
Figure 3.12 Sample taken from specimen with shear plane .....	72
Figure 3.13 Gypsification and adsorption contour for specimen with shear plane .....	73



## List of Tables

Table 3.1 Summary of undrained tests.....	54
Table 3.2 Summary of drained tests .....	54
Table 3.3 Water content distribution throughout specimen.....	66
Table 3.4 Adsorbed water content results that compare adsorbed water removal by $P_2O_5$ and by heat.....	67
Table 3.5 Summary of Water Content Analyses.....	72



# **1 Introduction**

## **1.1 Nature of Clay-Sulfate Rocks**

### ***1.1.1 Origin***

Shales are sedimentary rocks containing fine-grained sediments that have been strengthened by diagenetic bonding and by consolidation stresses much greater than the present overburden. Weathering processes produce clay minerals, which are eventually lithified into shales. Shales comprise nearly 80-95% of sedimentary rocks and, as with most sedimentary rocks, are primarily found on the outer “skin” of the earth’s crust (Bell, 1983).

Clay-sulfate rocks result when sulfates are introduced to shales. In fact, clay-sulfate rocks are very abundant because of the numerous sources of sulfate in the environment, both natural and anthropogenic. The natural environment where clay-containing sediments are deposited may be conducive to precipitation and deposition of sulfates species such as anhydrite. Also, sulfates may be leached from deposits, transported in solution over significant distances, and eventually reprecipitated in the pores of shales.

Shales are abundant at “shallow” depths of up to 10 km from the surface and are likely to contain sulfates, due to the many possible sulfate sources. Hence, clay-sulfate rocks are often encountered in construction and often serve as bearing stratum for deep foundations and waste repositories. It is therefore crucial to understand the engineering properties of clay-sulfate rocks and their behavior with respect to changes in the environment.

### ***1.1.2 Problems with clay-sulfate rocks***

The swelling behavior of clay-sulfate rocks is not as well understood as that of pure clay rocks. With conventional rock mechanics, the relationship between deformation and stress is

experimentally determined. Analysis of experimental results are then used to model the deformational behavior of rocks based on mechanical properties such as Young's modulus, Poisson's ratio, as well as laws for elastic, plastic, and creep behavior. This approach is valid as long as the changes in the rock are purely physical in nature. If there are chemical changes in the minerals, especially in the crystal structure of the rock matrix, conventional analysis of the deformational behavior of rocks could become more complicated (Zanbak & Arthur, 1986).

Clay-sulfate rocks cause problems in engineering applications due to the magnitude, delay, and irreversibility of their swelling behavior. As will be discussed in later sections, swell pressures generated by clay-sulfate rocks are at least twice that of clay or sulfate alone. Also, clay-sulfate swelling results in time-dependent deformations that tend to occur long after operation and construction efforts have started. Thus, delayed deformations can jeopardize the integrity of the structure, since supporting structures have already been constructed by the time deformations take place. Clay swelling involves the physical uptake of water, so swell heave in clay can often be suppressed by increase in overburden. Anhydrite swelling, on the other hand, is a chemical reaction, so clay-sulfate rocks may produce swelling that is most likely irreversible under normal testing conditions.

## **1.2 Clay Rock Behavior**

### ***1.2.1 Clay Swelling Mechanism: Adsorption***

Clay swelling is caused by the physical uptake of water that occurs simultaneously with or following stress relief. Exchangeable cations exist at the surfaces of clay particles. Upon contact with water, both the mineral surfaces and exchangeable ions pick up water. With their shells of water, ions can grow several folds in volume. The ions then move away from the

mineral surfaces to a position of equilibrium. On one hand, the ions are attracted to the negative charges within the mineral surfaces. At the same time, they also repel each other due to their thermal energies. As a result of these two forces, ions move away from the surface and into a new equilibrium position to form what is termed the double layer. The water in the double layer is under attractive force to the soil particle since this water is attached to exchangeable ions that are in turn attracted to the soil surface. Water is also attracted to the mineral surface by other forces, such as hydrogen bonding and van der Waals forces (Lambe & Whitman, 1969).

In the swelling process, the adsorbed water content is especially high for minerals with expandable layers. Figure 1.1 shows the sheet structures of common clay minerals. Minerals such as montmorillonite (also referred to as smectite) have expandable layers that allow for swelling, while minerals such as kaolinite only adsorb water externally. Water adsorption capacity in the vapor phase depends on specific surface, amongst other factors such as charge per unit cell and type of cation. Smectites are expandable clays and have the greatest surface area of all natural clay materials (Madsen & Nüesch, 1994).

### ***1.2.2 Strength of Shales***

Shales are formed in sedimentary basins by a process consisting of deposition, mechanical compaction and de-compaction (erosion), and diagenesis. During diagenesis, shales are cemented via precipitation of calcium carbonates, aluminum and iron hydroxides, or organic compounds at the interparticle contacts. Diagenesis also converts smectite to illite, i.e., as the level of diagenesis increases, the illite/smectite ratio also increases. In the end, young sediment is transformed into fully compacted and cemented shale. The strength of shale is dictated by properties of the original mud deposit, loading history, and mineralogical changes due to diagenesis. Gutierrez's (1996) correlation between shale strength (unconfined compressive

strength, effective peak friction angle, and undrained shear strength) with physical properties (porosity and Atterberg limits), mineral composition and stress history will be summarized below. This study used an assortment of different shales, the origin of which are not stated in the paper. From Atterberg limits, most of the shales fall within the boundaries set by the A-line and the U-line, which indicates that most of the material can be classified as CL (low to medium plasticity clays) according to the USCS system.

#### 1.2.2.1 Physical Properties

The correlation of peak friction angle<sup>1</sup>  $\phi$  with porosity  $n$  and plasticity index  $I_p$ , are shown in Figures 1.2 and 1.3. Despite the large scatter, the data does indicate a trend of decreasing friction angle with increasing porosity and plasticity index, as expected. The reduction in friction angle with increasing plasticity index is in close agreement with the correlations for undisturbed clays by Bjerrum and Simons (1960).

#### 1.2.2.2 Mineral Composition

Laboratory tests show no clear relationship between mineralogical content and strength. In theory, higher illite content should result in higher degree of diagenesis and cementation, and thus, higher strength. But, the data in Figures 1.4-1.6 show the difficulty of correlating illite content with friction angle and strength properties.

#### 1.2.2.3 Stress History and Diagenesis

Shales exhibit apparent pre-consolidation stresses, which have a mechanical component and a diagenetic component. Though much more scattered as compared to soil data, Figure 1.7 shows that there is a clear trend of increasing normalized undrained shear strength with

---

<sup>1</sup> The paper does not specify the type of test from which the friction angle is estimated.



increasing OCR for shales. The SHANSEP -- Stress History and Normalized Soil Engineering Properties -- procedure of Ladd & Foott (1974) can be used to describe shale behavior:

$$\frac{s_u}{\sigma'_{vc}} = S (OCR)^m$$

where  $s_u$  is the undrained shear strength,  $\sigma'_{vc}$  is the effective vertical consolidation stress,  $OCR$  is the overconsolidation ratio,  $S$  and  $m$  are empirical constants. The overconsolidation ratio is defined as:

$$OCR = \frac{\sigma'_{vmax}}{\sigma'_{vc}}$$

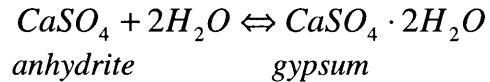
where  $\sigma'_{vmax}$  is the apparent maximum vertical effective stress that the shale has been subjected to. The average constants for several shales are  $s=0.29$  and  $m=0.93$ . In some shale samples, the pre-consolidation stress appears to be too high to be due to stress-induced compaction alone. According to Jones and Addis (1985), the expected maximum burial stresses for most shales rarely exceed 10 MPa. Thus, the apparent maximum pre-consolidation stress of shales must be dictated by more than just the maximum past burial stress.

Although there is limited data, it can be postulated that increase of shale strength due to diagenesis can appear as increase in apparent pre-consolidation. Figures 1.8 and 1.9 show data relating the degree of diagenesis with apparent maximum past pressure; Gutierrez (1996) measures diagenesis using illite content, while the McKown and Ladd (1982) study uses calcium carbonate content. In shale deposits where the geological history is unclear, it is not possible to separate the mechanical pre-consolidation from increase in pre-consolidation due to diagenesis-induced cementation. Thus, at present, it is not possible to quantitatively relate the increase in pre-consolidation with degree of diagenesis.

## 1.3 Sulfate Behavior

### 1.3.1 Anhydrite Swelling Mechanism: Gypsification

In nature, calcium sulfate exists in two forms: anhydrite and gypsum. Anhydrite minerals swell via hydration, i.e. the chemical transformation of anhydrite to gypsum:



Anhydrite is not transformed directly to gypsum upon contact with water. Instead, the anhydrite dissolves in water and gypsum precipitates out of the solution accordingly; Posnjak (1938) found the solubility of anhydrite in pure water at 25°C to be 2.7g/L, while that of gypsum is about 2.4g/L. The gypsum-anhydrite equilibrium temperature in pure water is around 58°C; gypsum is stable below 58°C, while anhydrite is more stable above 58°C (Hardie, 1967).

Gypsification results in a maximum volume increase of 60% for completely dry, voidless anhydrite that has been exposed to water in an open system (Madsen & Nüesch, 1991). An open system is defined as an environment where water may freely enter the system in the hydration process. The magnitude and rate of conversion depend on factors such as surface area exposed to water, availability of water, and stress level. Since gypsification takes place at the surface, massive anhydrite with few cracks does not swell as substantially as finely ground anhydrite.

In nature, hydration of an anhydrite layer can be constrained by internal pressure build up or gypsum crust formation. For buried anhydrite layers with some porosity, volume increase due to hydration will cause partial or complete loss of porosity. Excess swell stress that is not absorbed by the gypsum layer will then be transmitted onto the host rock. Depending on the E modulus and Poisson's ratio of the host rock, the excess strain may create excess stresses on the host rock. The effect of the extra stresses on the host rock affects the magnitude of the hydration

process. Specifically, if the host rock is very compressible, the entire anhydrite layer may be converted into gypsum, which can cause further consolidation of the host rock mass. If the host rock is stiff, the confining stress on the anhydrite/gypsum layer may increase to a level where further volume increase cannot be accommodated and hydration ceases (Zanbak & Arthur, 1986).

In addition to external stresses, the hydration process can also be constrained by the formation of gypsum crusts. Gypsum crusts produced at the upper and lower boundaries of the anhydrite layers create a barrier with low hydraulic conductivity, which will decrease and eventually cease hydration (Zanbak & Arthur, 1986).

## **1.4 Clay-Sulfate Behavior**

### ***1.4.1 Clay-Sulfate Swelling***

A combined swelling mechanism occurs in rocks containing both anhydrite and clay. However, the volume increase of clay-sulfate rocks is more severe than that of either clay or anhydrite alone. As discussed above, anhydrite alone is capable of 60% volume increase but may be limited by internal pressure buildup or gypsum crusts. In the combined swelling mechanism, the clay provides continuous supply of water through its pores to anhydrite that may be located in the inner portions of the rock mass. The combined swelling mechanism is particularly severe if clay and anhydrite are in alternate layers. Madsen & Nüesch (1991) found that the maximum swelling stress occurs in rocks containing 10-15 % clay and 70-75% anhydrite (Figure 1.10).

In addition to the severity, the duration of the swelling process for clay-sulfate rock is also much longer than that of clay rock. Clay-sulfate rocks show an immediate rapid volume

increase due to water adsorption by clay, followed by a slow but steady volume increase due to anhydrite swelling. Figure 1.11 shows the evolution of swelling stresses for anhydrites and shales. The data indicates that clay swelling in the shale sample is completed after 2 weeks, while anhydrite swelling continues even after 2000 days. Figure 1.11 also shows that the shaley anhydrite reaches swelling stresses more than twice that of the other samples.

The gypsification reaction front is controlled by the accessibility of water. In clay-sulfate rocks, inflow of water is dependent on the distribution of anhydrite and clay. Gypsification is concentrated in areas rich in clay minerals. Gypsum crystals adjacent to clay minerals often show a fine-grained margin, which is assumed to be a reaction seam. Specimens show that the reaction front ends where the clay content diminishes. It is apparent that clay plays a catalytic role in the anhydrite/gypsum transformation.

The gypsification in clay-sulfate rock progresses via a crack and seal mechanism. Water circulation within a layer of clay is much greater than that across the layer. For gypsification to spread beyond the clay layer, the swell pressure of gypsum formation must exceed the strength of the material. Consequent development of new cracks allows water access and further gypsification. Several phases of this crack and seal process lead to a net transport of marginal gypsum through veins and into the interior of the material.

The structure and texture of clay-sulfate rocks influence the flow of water into the rock and, consequently, the extent of gypsification. Figure 1.12 shows the stepwise increase in swell stress over four years. After four years, samples still have high anhydrite content, which can be attributed to the crack and seal mechanism: With cracks propagating into the anhydrite, swelling stress rises until the surrounding anhydrite is converted to gypsum, resulting in a “gypsum seal”. The sealing process reduces porosity, hydraulic conductivity, and thus water accessibility. Over

time, water infiltration diminishes and gypsification ceases. Thus, at the conclusion of the swell stress tests, specimens may still have relatively high anhydrite content. The crack and seal mechanism also prolongs the swelling process and is therefore responsible for the long duration of the swell stress tests (Nüesch et. al., 1995).

#### ***1.4.2 Deformational Behavior of Clay-Sulfate Rocks***

Within strained shale-sulfate multilayers, two types of deformation regimes can be found. Rocks may exhibit ductile or brittle behavior. Jordan & Nüesch (1989) report that deformation type – ductile or brittle -- is influenced by confining pressure and water content. They also propose that temperature should have little effect on deformation regime, except at  $T > 200^{\circ}\text{C}$ , where dehydration and embrittlement occurs.

Ductile failure is characterized by pervasive deformations that result in large-scale shale cataclases, commonly rich in gypsum. Specifically, dilation results in new pore space, which is subsequently filled with gypsum. Generally, this process nucleates in a discrete shear zone. But the shear zone becomes increasingly broader with increasing strain, such that, eventually, the material behaves as a nearly homogeneous medium.

In brittle failures, strain is strongly concentrated along discrete surfaces. Slickensides are shear surfaces coated with sulfate that acts as a lubricant. The slickensides in shales are characterized by highly polished, mostly planar surfaces. The slickenside surfaces are produced by very strong preferred orientation of the platy clay minerals or mineral aggregates, typically parallel to the shear surface. The thickness of the slickenside domains normal to the surfaces range from 1 to 4  $\mu\text{m}$ . In these zones, the packing of clay material is distinctly denser than in the nearby domains. Furthermore, the average grain size of clay aggregates decreases near the slickenside surface. In summary, this deformational regime can be described as cataclasis along

narrow discrete shear zones, which result in grain-size reduction and progressive alignment of clay minerals or mineral aggregates parallel to the shear-zone boundaries (Jordan & Nüesch, 1989).

## **1.5 Applications of Clay-Sulfate Rocks**

The significance of clay-sulfate rock lies in its ubiquity and potential applications. In tunnel and other forms of underground construction, encounters with clay-sulfate material may be inevitable. The swell heave of clay sulfate rock surrounding a tunnel may result in immense swell stresses that induce cracking and endanger the integrity of these infrastructures over the years.

Due to their abundance at the Earth's surface, clay-sulfate rocks can also affect operations such as geothermal energy extraction – the extraction of heat from the Earth's interior through very deep boreholes. Geothermal extraction is important for global sustainability since it makes use of a practically inexhaustible renewable energy source. The high deformability and swelling behavior of clay-sulfate rocks can make it difficult to keep the drill holes open during the extraction process.

Clay-sulfate rocks can serve as barriers that isolate hazardous materials from the biosphere. In these repositories, the waste is modified through decay and interaction with the clay minerals. Shales have low hydraulic conductivity; Brace (1980) cites the hydraulic conductivity of shales to be in the range of  $10^{-6}$  to  $10^{-11}$  darcy. Furthermore, clays have small diffusion coefficients and high adsorption capacity for organic compounds and heavy metals. The swelling behavior of clays adds to the retention capabilities of clay liners by decreasing the hydraulic conductivity of the liners. Clays also cause precipitation and deposition of minerals

from waste leachates, which may increase mechanical retention, reduce pore space, and consequently, decrease hydraulic conductivity. Thus, clay shales possess the necessary properties to be competent barriers for waste repositories.

Unlike clay shale barriers, clay-sulfate rocks have the capability to self-heal in the event of fractures or cracks. Geological barriers are endangered mainly by squeezing, swelling, and deformation processes that cause cracks and fractures, which create distinct water paths that could connect waste sites with the biosphere. Therefore, a self-sealing mechanism, which starts immediately following rupture, is an important quality for a host material. Gypsum has the ability to dissolve and reprecipitate in cracks of brittlely deformed shale, which makes clay-sulfate rocks an ideal building material for repositories (Nüesch & Ko, 1997).

Though characterized by self-healing capabilities, clay-sulfate rocks are at the same time more likely to crack/fracture than pure shales due to large volume increases related to swelling. The behavior of this material in the field depends on the outcome of these competing forces. Thus, laboratory testing is necessary to understand what exactly happens to this material under different stress conditions.

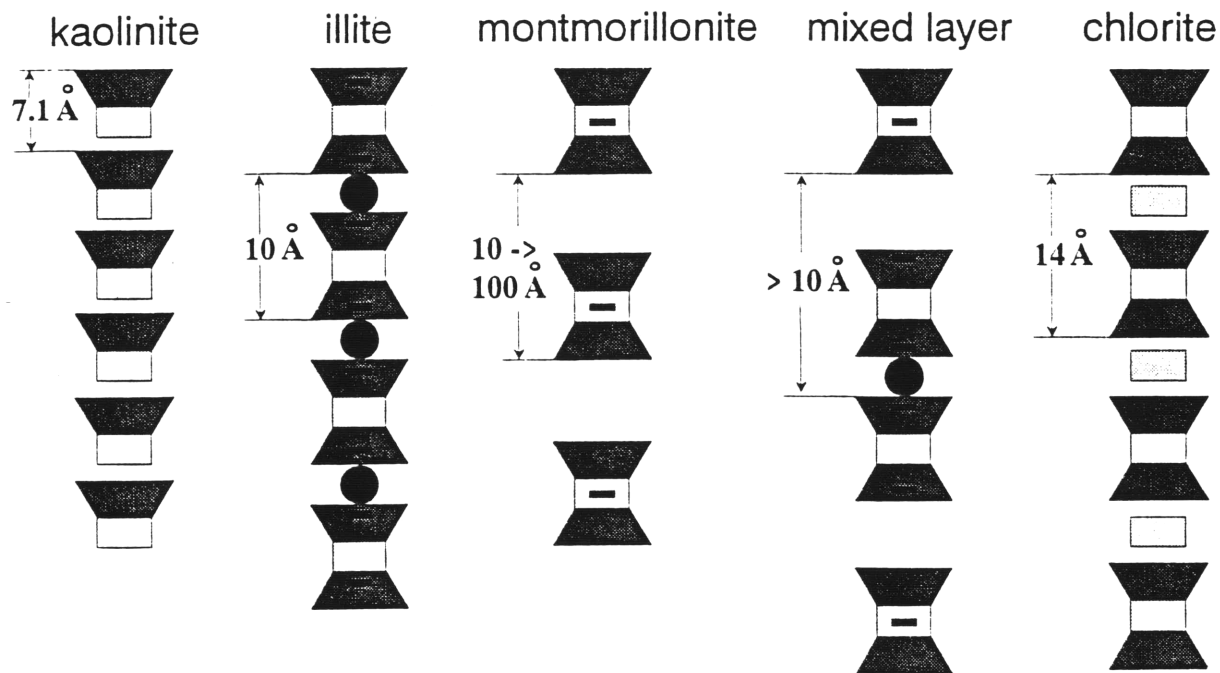
## **1.6 The Testing Program**

The goals of this testing program are

- 1) to characterize the undrained strength of reconstituted clay-sulfate rock (15% clay and 85% anhydrite, compressed under 100 MPa) and
- 2) to assess the effect of shear on gypsification.

A series of undrained and drained conventional triaxial compression tests will be performed at different consolidation stresses and shear rates. After shearing, water content analysis will be used to determine gypsification levels.





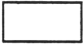
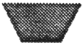



-  Octahedral layer with aluminum atoms
-  Tetrahedron layer with silicon atoms
-  Octahedral layer with possible substitution of  $\text{Fe}^{3+}$  or  $\text{Mg}^{2+}$  for  $\text{Al}^{3+}$
-  Tetrahedron layer with one-fourth of  $\text{Si}^{4+}$  replaced by  $\text{Al}^{3+}$
-   $\text{K}^+$

Figure 1.1 Sheet structures for several common clay minerals. (Claylab, IGT)

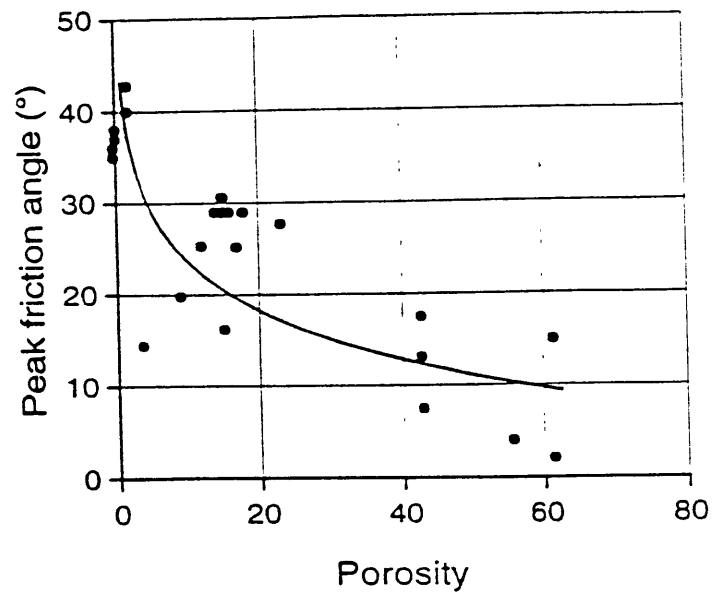


Figure 1.2 Peak friction angle as a function of porosity for different shales. (Gutierrez et. al., 1996). Porosity measured in %.

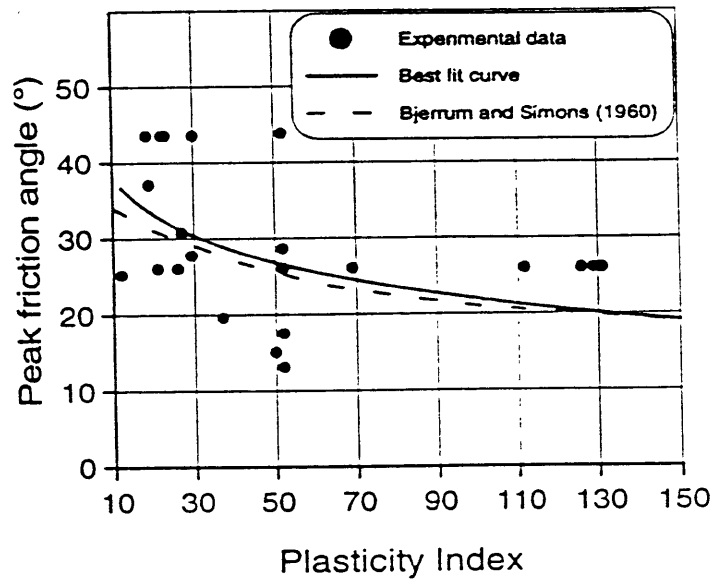


Figure 1.3 Peak friction angle as a function of plasticity for different shales. (Gutierrez et. al., 1996)

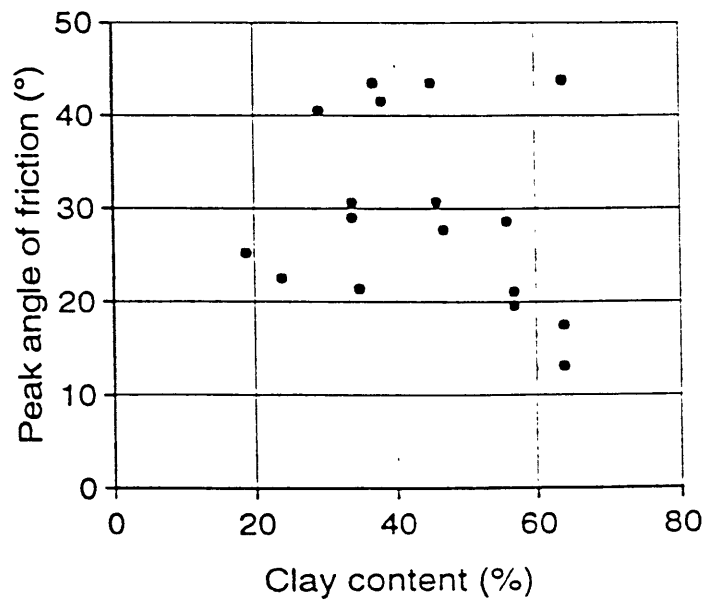


Figure 1.4 Peak friction angle versus clay content for different shales. (Gutierrez et. al., 1996)

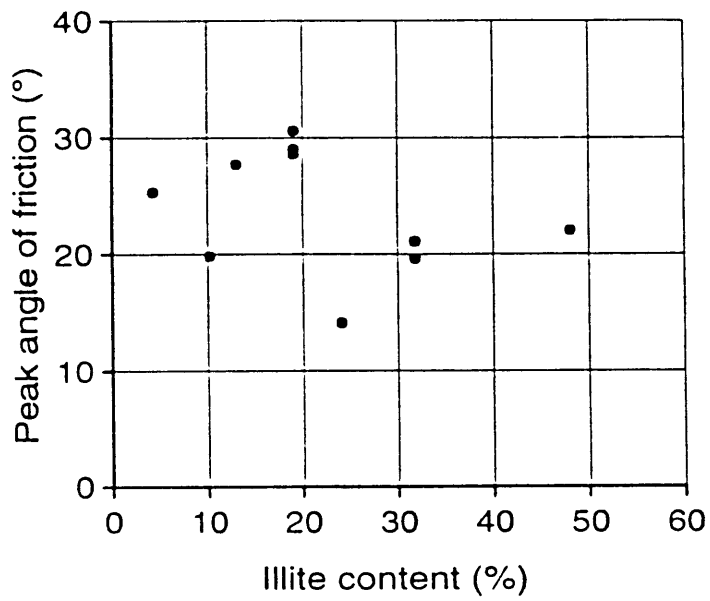
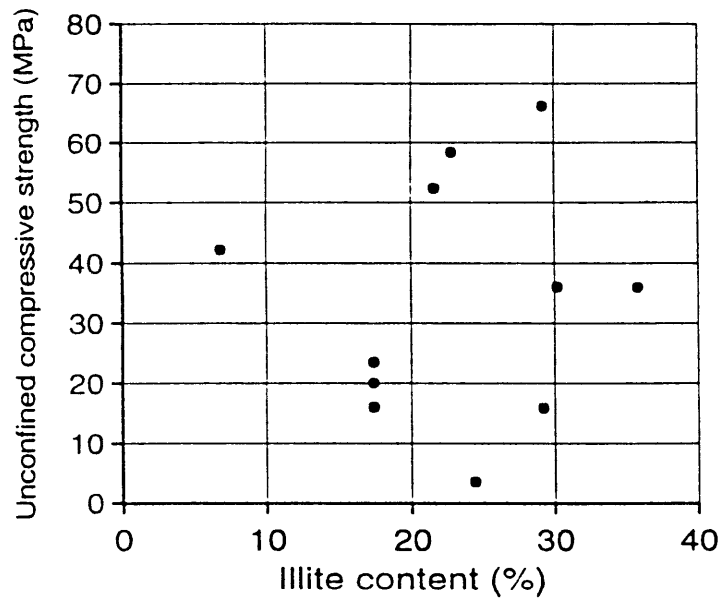


Figure 1.5 Peak friction angle versus illite content for different shales. (Gutierrez et. al., 1996)



**Figure 1.6 Unconfined compressive strength versus illite content for different shales. (Gutierrez et. al., 1996)**

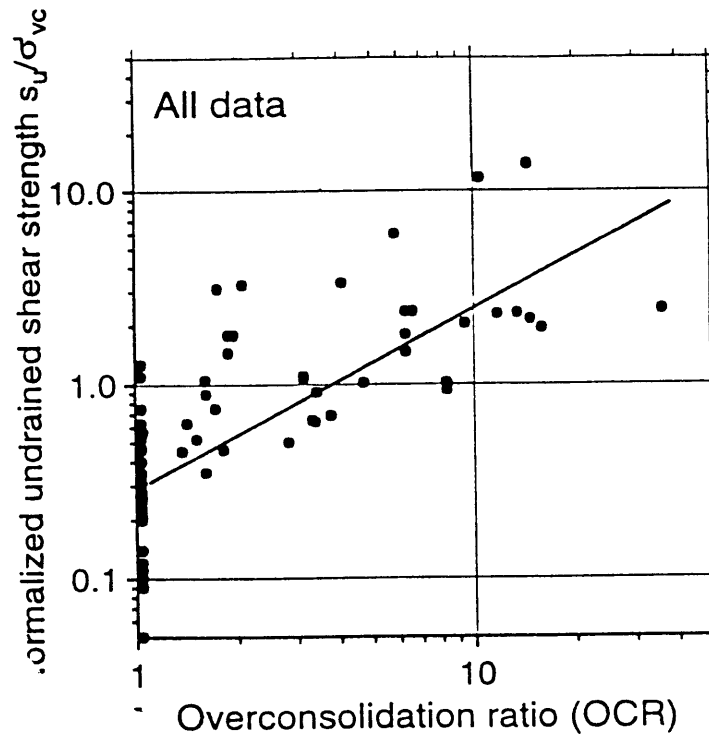


Figure 1.7 Normalized undrained shear strength as a function of OCR for different shales. (Gutierrez et. al., 1996)

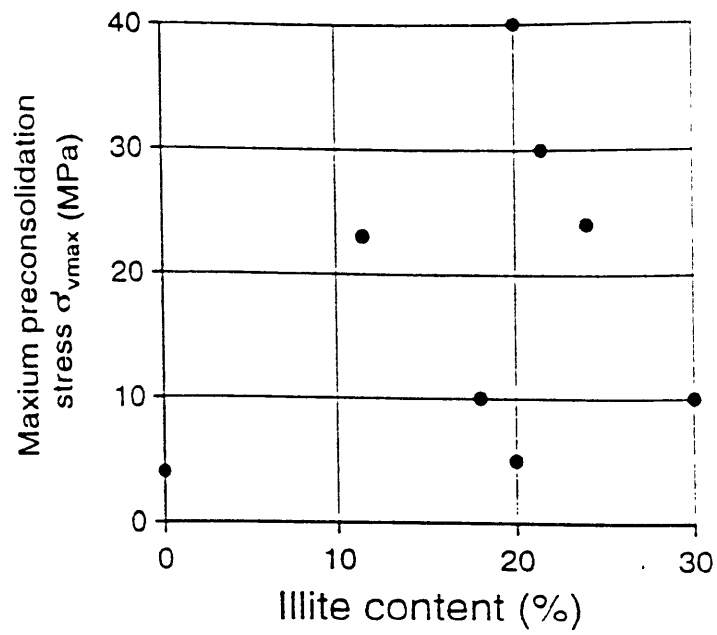


Figure 1.8 Maximum apparent pre-consolidation stress as a function of illite content for different shales. (Gutierrez et. al., 1996)



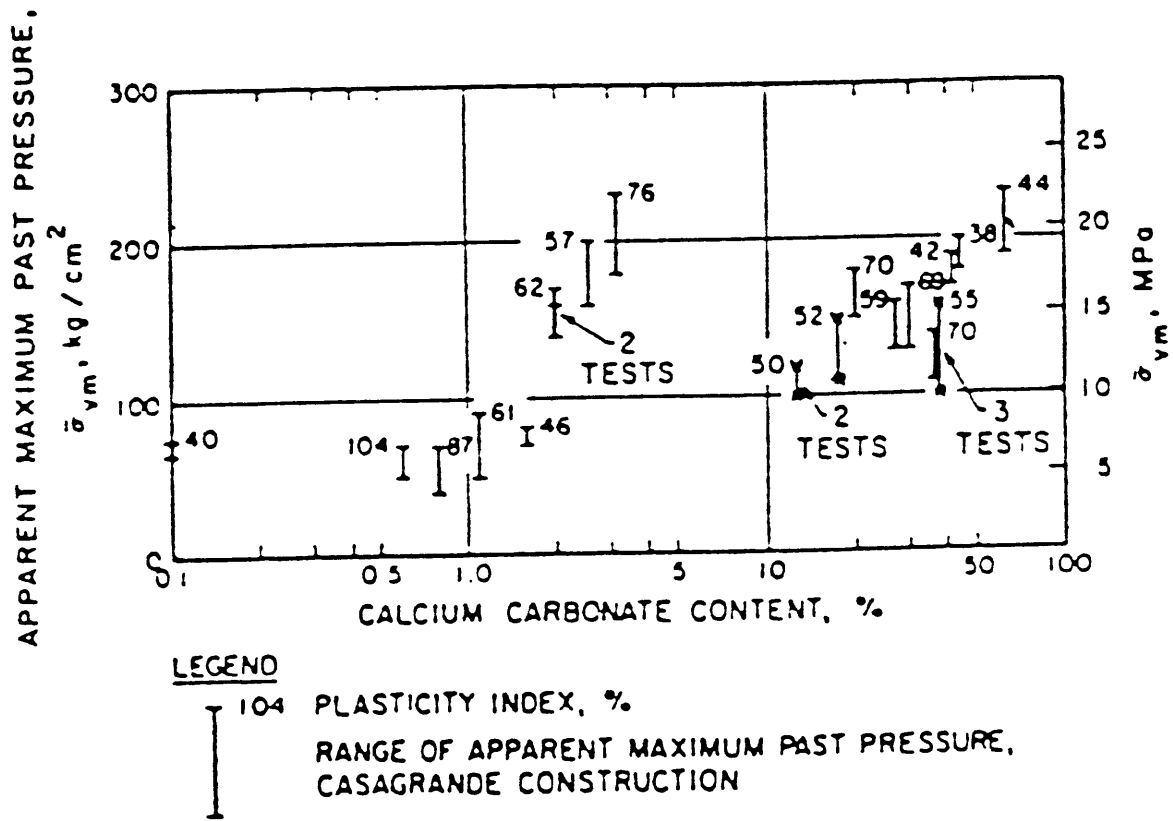


Figure 1.9 Maximum apparent pre-consolidation stress obtained from one-dimensional consolidation tests as a function of CaCO<sub>3</sub> for Pierre shale. (McKown and Ladd, 1982)

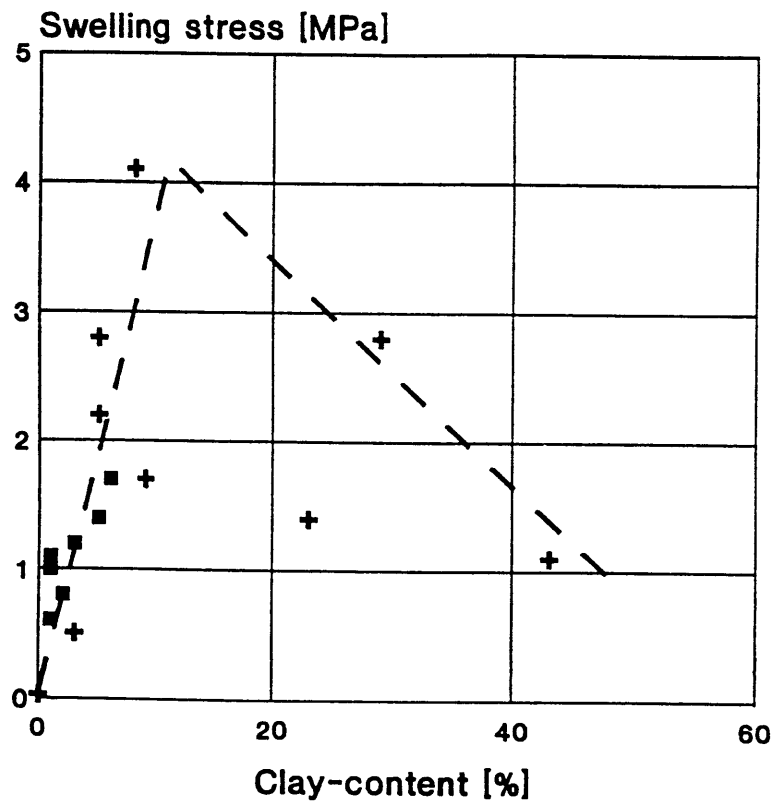


Figure 1.10 Swelling stress versus clay content at 600 days of testing. (Madsen & Nüesch, 1991)

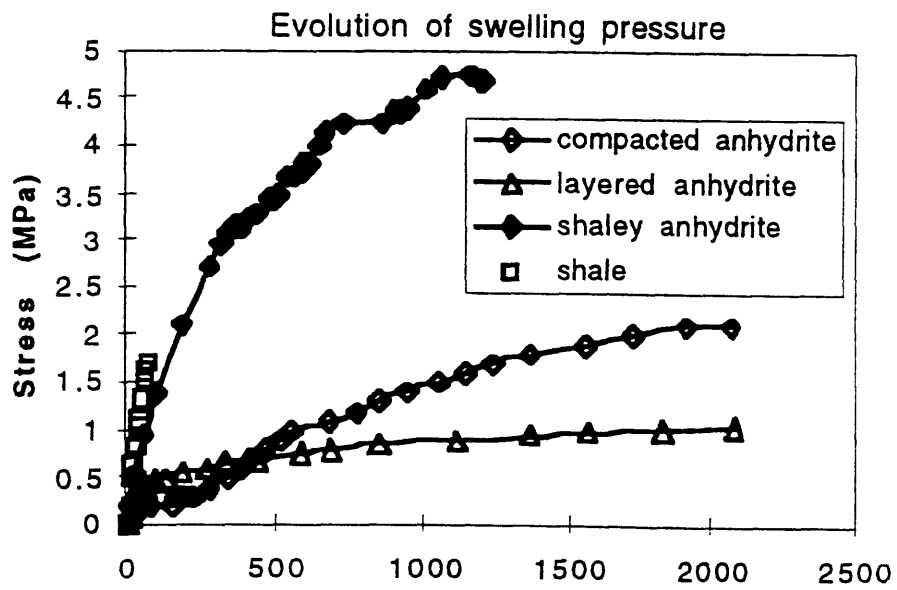


Figure 1.11 Time-dependent swelling of shale, anhydrite (massive, crushed, and pressed) and shaley anhydrite rock. Time (on x-axis) is measured in days (Nüesch & Ko, 1997)

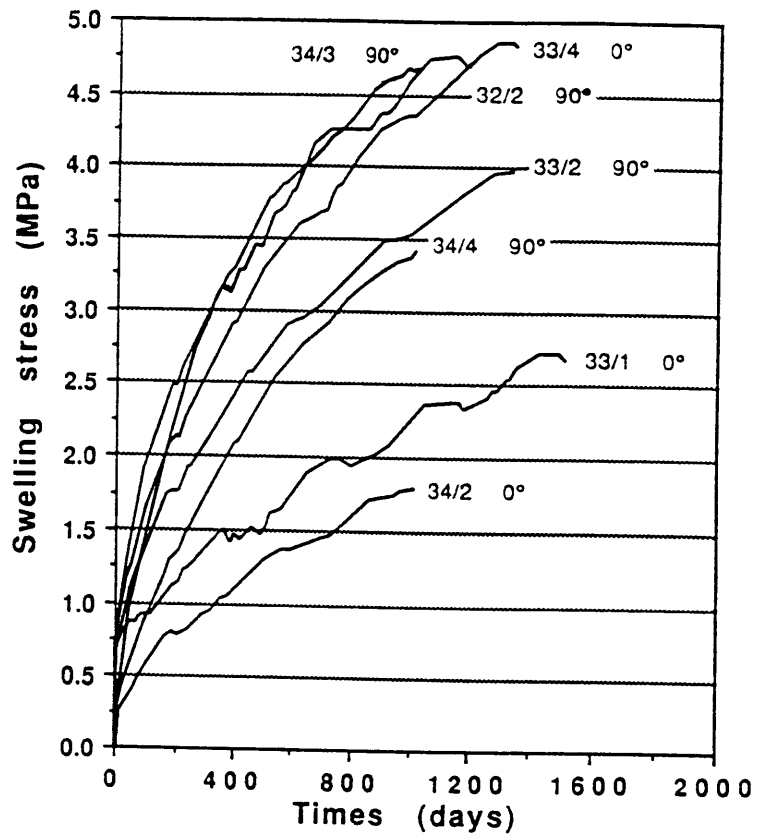


Figure 1.12 Stepwise swelling stress increase over time for clay-sulfate rock specimens. (Nüesch & Madsen, 1995)

## 2 Materials and Procedures

The engineering properties of clay-sulfate rocks are determined through a laboratory-testing program. This chapter describes the procedures used to determine the strength and deformability of reconstituted clay-sulfate rock. A series of triaxial tests are performed to determine the strength characteristics. Though both drained and undrained shear tests were performed, the tests are predominantly unconsolidated undrained compression tests. After triaxial testing, specimens are further analyzed for gypsum content.

### 2.1 Nature of Testing Material

The Clay Mineralogy Laboratory at ETH<sup>2</sup> prepared the synthetic specimens used in this testing program. Reconstituted specimens provide better control of factors such as clay/anhydrite composition, porosity, maximum past pressure, and reproducibility.

#### 2.1.1 Mineralogy and Sample Preparation Method

The reconstituted rocks originate from anhydrite and montigel powder. Anhydrite is the unhydrated form of calcium sulfate,  $\text{CaSO}_4$ . Montigel, a commercial form of bentonite, is composed of Ca-montmorillonite.

To prepare the specimens, anhydrite and montigel powders are mixed at room temperature and atmospheric pressure. The samples used in this testing program consist of 15% montigel and 85% anhydrite, by weight. The powder mixture is placed in a pressure cell and cold pressed at 100 MPa overnight. The solidified material is then shaved into cylinders with a lathe. The specimens are typically 3.5 cm in diameter and 5.0-5.8 cm in height.

---

<sup>2</sup> Eidgenössische Technische Hochschule (Zürich, Switzerland)

## 2.2 Triaxial Testing Equipment

### 2.2.1 The Triaxial Cell and Load Frame

The triaxial cell used in this testing program was originally manufactured by Wykeham Farrance England, Ltd. Modifications were made to allow for top drainage and to accommodate an internal load cell. When fully assembled, the cell is about one foot tall. Figure 2.1 shows the main components of the cell.

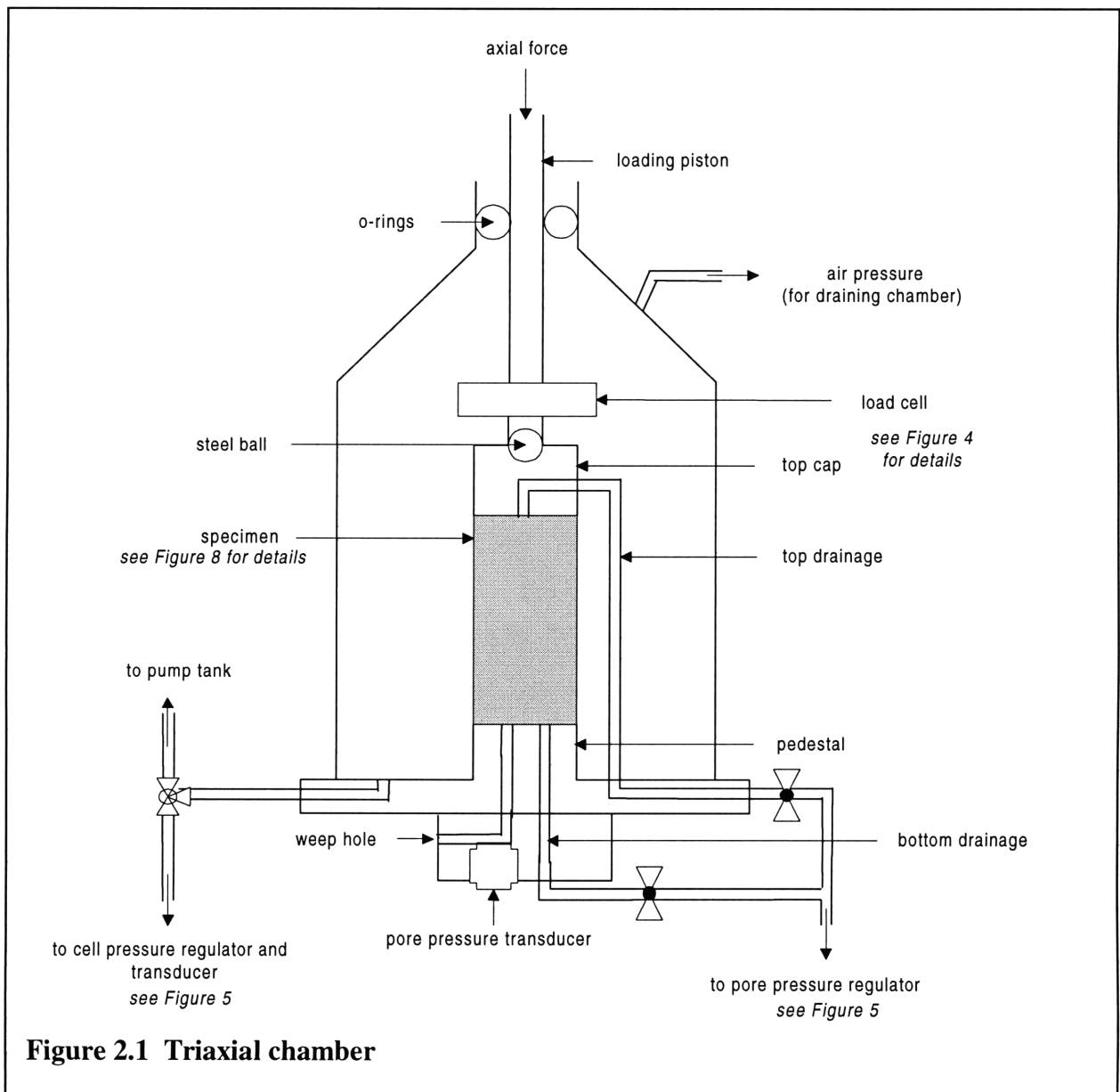


**Figure 2.1 Triaxial chamber**

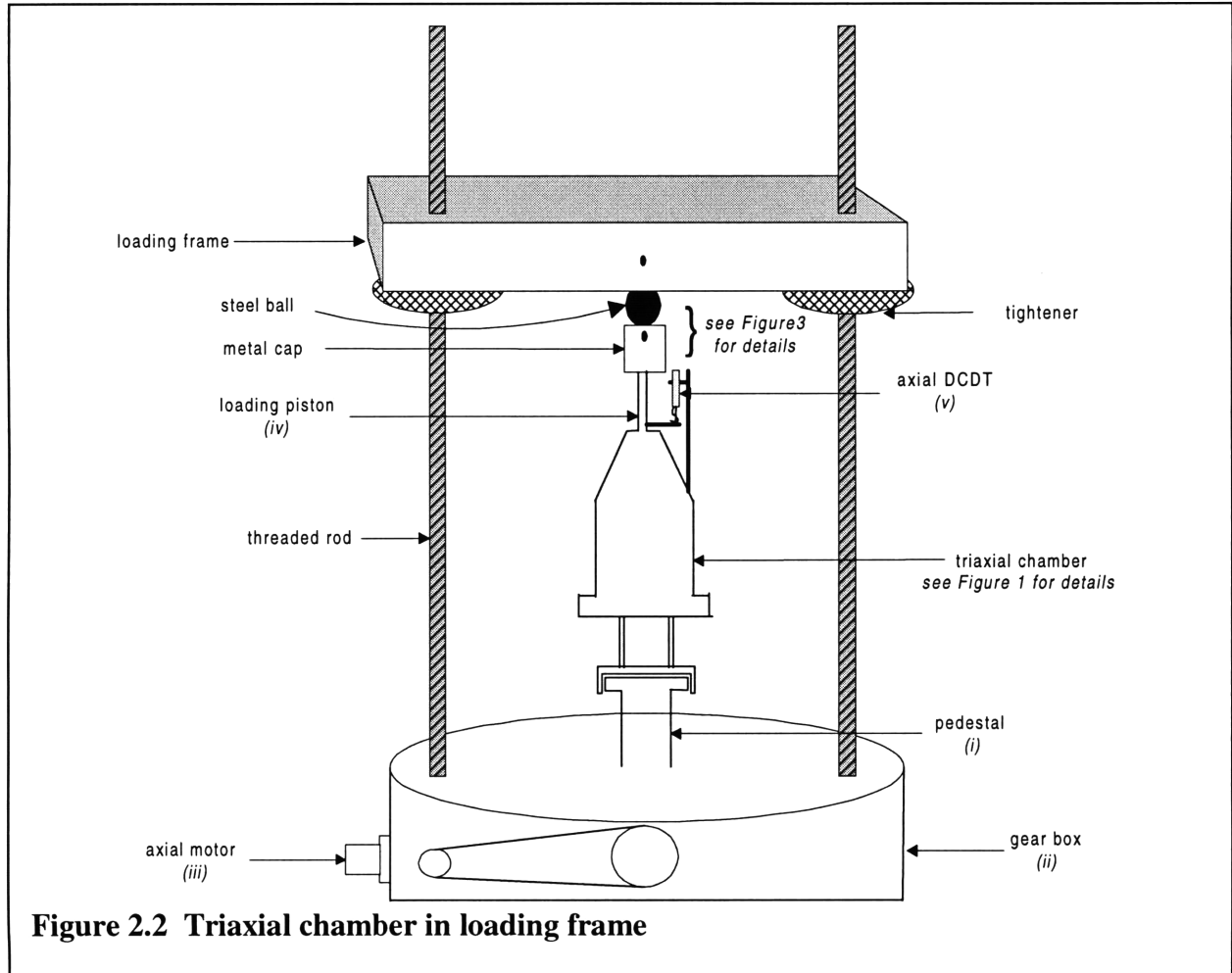
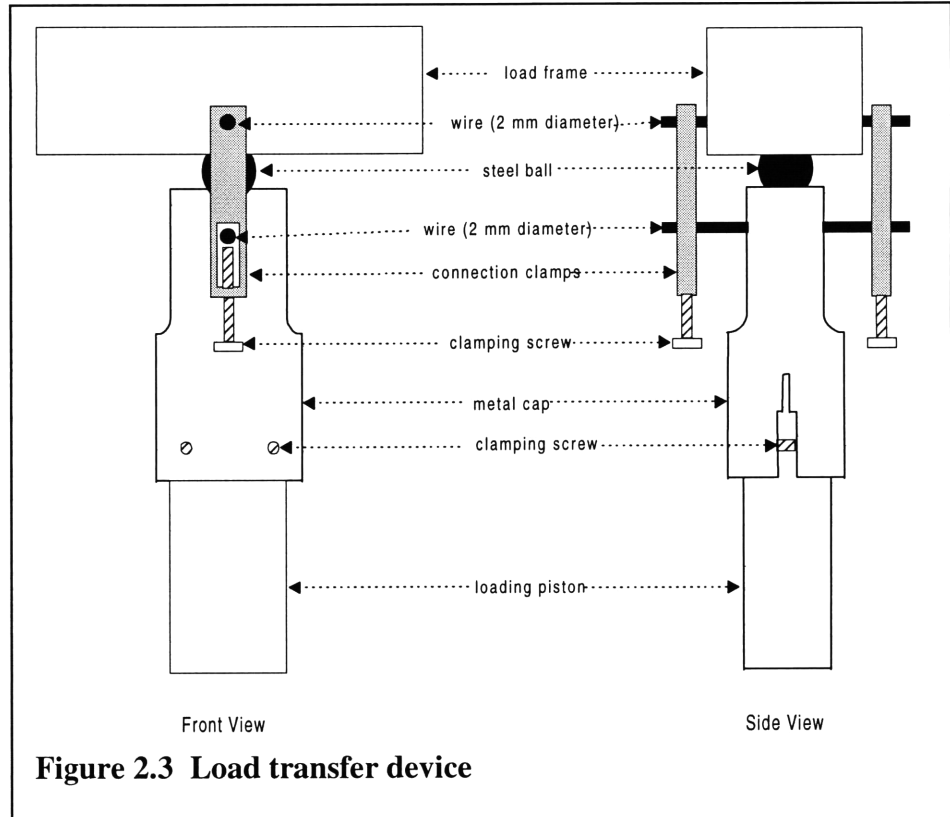


Figure 2.2 shows the triaxial cell in the mechanical loading frame. The triaxial chamber sits on a loading pedestal (i), which is raised and lowered through a five-position gearbox (ii). The axial servo motor (iii) drives the input gear of the five-position gearbox. A loading piston (iv) slides freely through an opening at the top of the cell. Hence, as the pedestal moves the chamber up, the loading piston applies axial load on the specimen (Figure 2.1). A DCDT (TRANS-TEK: model# 0243-0000) is anchored to the chamber and measures the displacement of the loading piston, from which axial strain is calculated (v).

To perform both triaxial compression and extension tests, it is necessary for the load frame to be able to deliver compressive as well as pick-up load. A load transfer device (LTD) was developed by Dr.

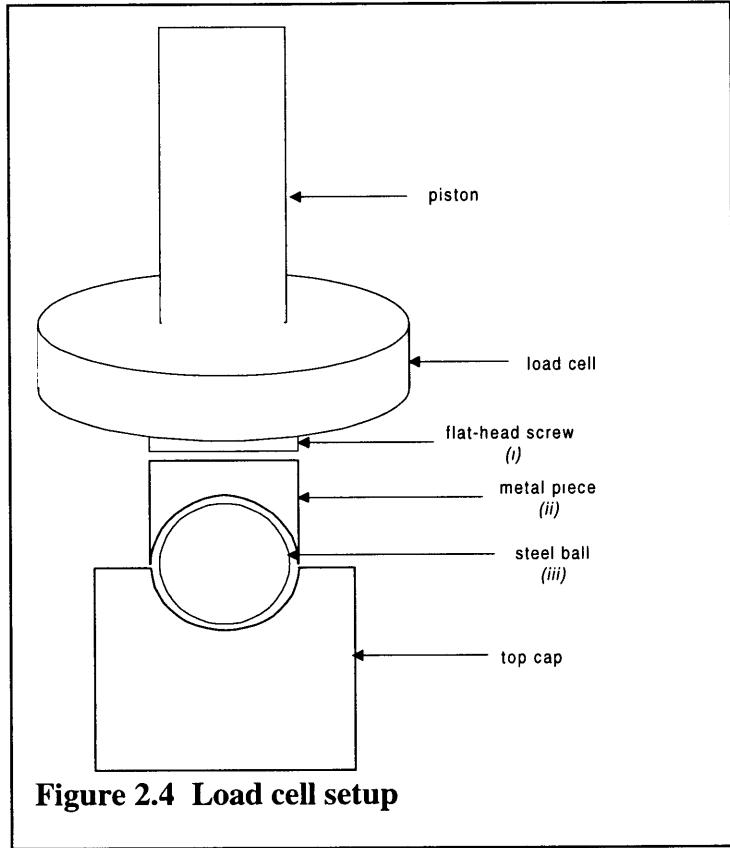


John T. Germaine to connect the loading piston and the load frame. Figure 2.3 shows the detailed components of the LTD. A metal cap is connected to the loading piston, which is secured to the load frame through a system of connection clamps and wires.

A load cell (Kulite Semiconductor, Inc: TC-2000, 2500 lbs.) is screwed onto the loading piston and rests on the top cap as shown in Figure 2.4. A flat-headed screw (*i*) is fixed on the bottom of the load cell, such that the head of the screw (0.23" thick) protrudes from the bottom of the load cell. A 0.5" diameter steel ball sits in a groove that is cut into the top cap. A piece of metal (*ii*) is shaped to fit over the steel ball (*iii*) on one end and flattened to make contact with the flat-headed screw on the other end. When submerged in the triaxial chamber, the load cell is insensitive to variations in the cell pressure. Due to its location, the submersible load cell does not measure axial forces due to piston friction.



The pedestal and top cap are both 3.5 cm in diameter. Holes in the pedestal and the top cap provide bottom and top pore drainage, respectively. In addition to the drainage hole, there is an adjacent hole in the pedestal that leads to the pressure transducer (Data Instruments: model AB HP, 2000 psi), which is positioned at the base of the cell (Figure 2.1). Pore water drainage in the top cap is provided by a hole



that connects to metal tubing, which leads to a drainage hole at the base of the cell. The top and bottom drainage lines merge into a single tubing that leads to the pore pressure regulator (Figure 2.1); two shutoff valves isolate the drainage lines (and thus the sample) from the pressure regulator.

### 2.2.2 Pressure-Volume Controllers

During triaxial tests, pressure needs to be applied and maintained in the cell (confining pressure) and sometimes in the specimen (back pressure). Pressure-volume controllers or PVCs are used to physically adjust the cell and pore pressures. The PVC is a hydraulic pressure source that can be operated manually or through computer control. Figure 2.5 shows the primary components of the PVCs. Though the hydraulic fluids are different, the PVC for the cell pressure and the pore pressure are functionally identical. As shown in Figure 2.5, the piston (vi)

is sealed with two O-rings in the end cap of the hydraulic cylinder (vii) and connected to a threaded shaft (v). The PVC is powered by a DC servo motor (iii). This motor drives worm gear 2, which turns an adjacent worm gear 1 positioned perpendicular to the first. The rotary motion of the worm gear 1 is translated to linear motion of the threaded shaft using high efficiency rotation ball bushings (not shown). The trailing section of the threaded shaft travels inside a protective sleeve (iv).

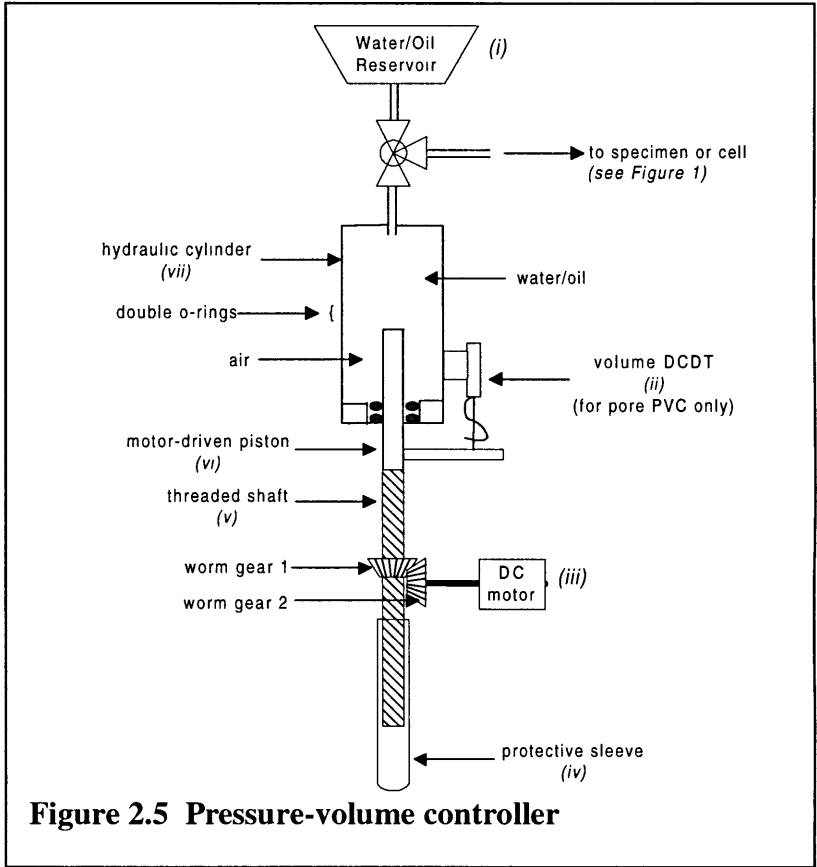


**Figure 2.5 Pressure-volume controller**

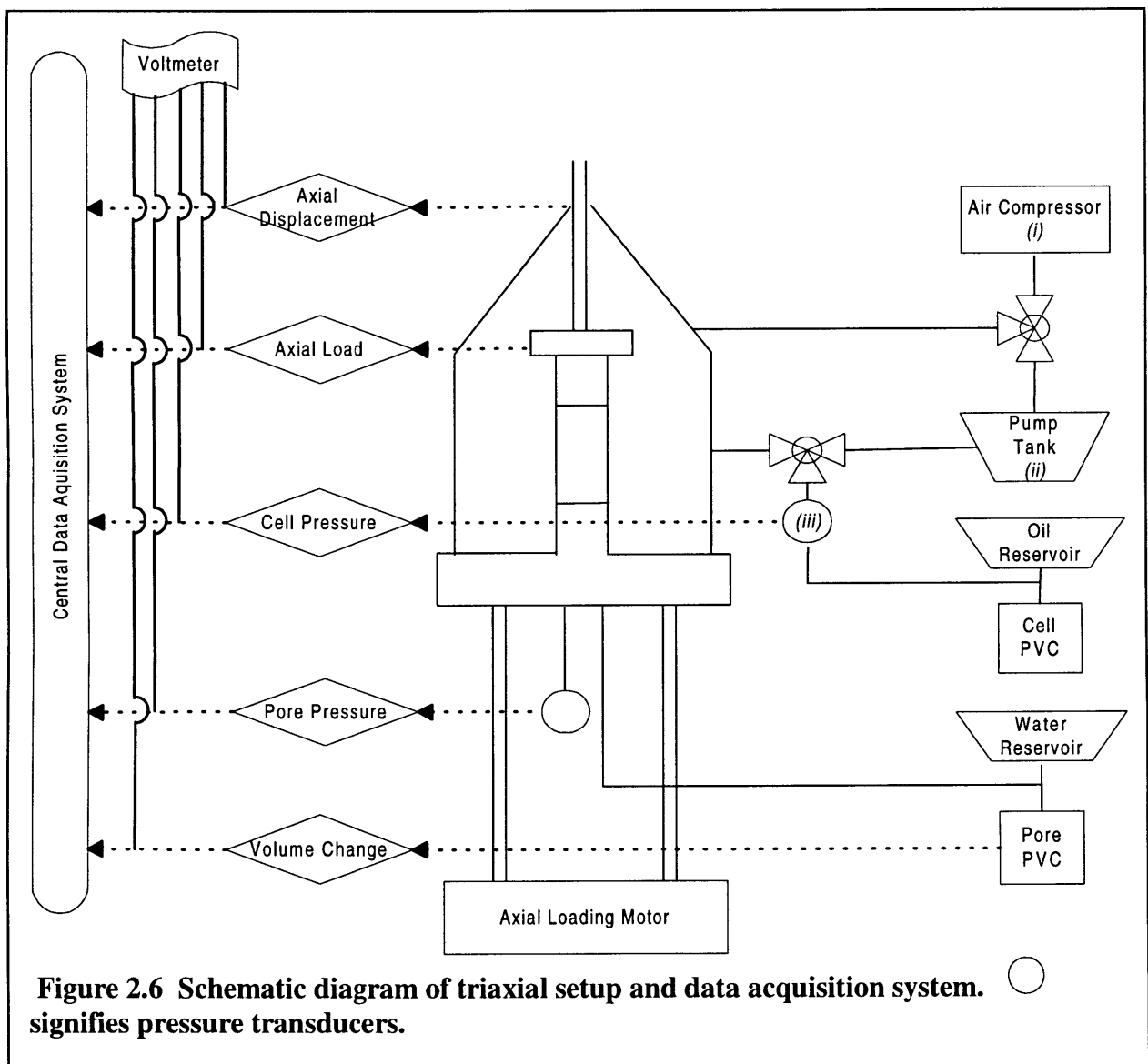
efficiency rotation ball bushings (not shown). The trailing section of the threaded shaft travels inside a protective sleeve (iv).

The hydraulic cylinder for cell pressure control is filled with silicon oil, while that for pore pressure control is filled with water. As shown in Figure 2.5, a three-way valve connects the cylinder to the reservoir (i) and the specimen/cell; when opened to the reservoir, the hydraulic cylinder can be refilled by drawing fluid from the reservoir. The hydraulic cylinder for the cell pressure is directly connected to the fluid inside the triaxial chamber. The hydraulic cylinder for the pore pressure is directly connected to the fluid inside the specimen; a DCDT (ii) (TRANS-TEK: model# 0244-0000) is fixed on the pore hydraulic cylinder to measure the movement of the piston, which can be used to calculate the volume of water that enters or exits the specimen. Through the worm gears and threaded shaft, the DC motor pushes or pulls the

piston. Since the fluid chambers are directly connected to the pressure lines, the piston movement can increase or decrease the pressure in the chamber and the specimen.

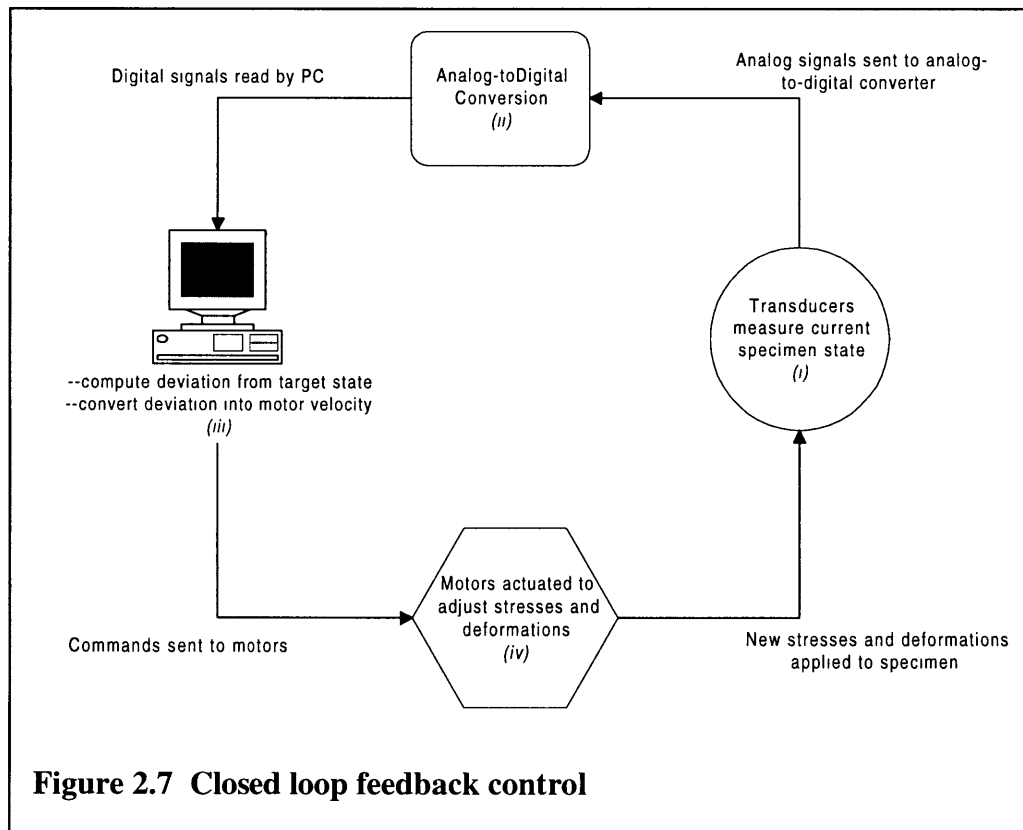
### 2.2.3 Computer Control

Figure 2.6 shows a schematic view of the measurement instrumentation. For the purposes of this study, five transducers monitor the stress-strain state of the specimen; all of the transducers use a DC input voltage of 5.5 volts, which is provided by a regulated power supply. All transducer signals as well as the input voltage are monitored and logged by the Central Data



## Acquisition System.

All tests are controlled through a Hyundai Super-16TE computer. Figure 2.7 maps the feedback control loop used in the computer-controlled tests. The first step of the loop is to take transducer readings (and input voltage) and compute the specimen's actual stress-strain state (i). The analog transducer signals are then converted into digital signals by an AD1170 A/D converter (ii). Specifically, a digital representation of the analog voltage consisting of a "bit-count" is produced and sent to the AD1170 microcomputer's memory; the "bit-count" is a fraction of the total number of bits that corresponds to full range. After voltages have been retrieved and stress-strain state of the specimen computed, the computer control software compares the actual engineering quantities to the target values (iii). A software control algorithm then computes the motor speeds necessary to maintain the target stress-strain state (iv); there are three motors that control the stress-strain state – axial motor (Figure 2.2, (iii)), cell PVC

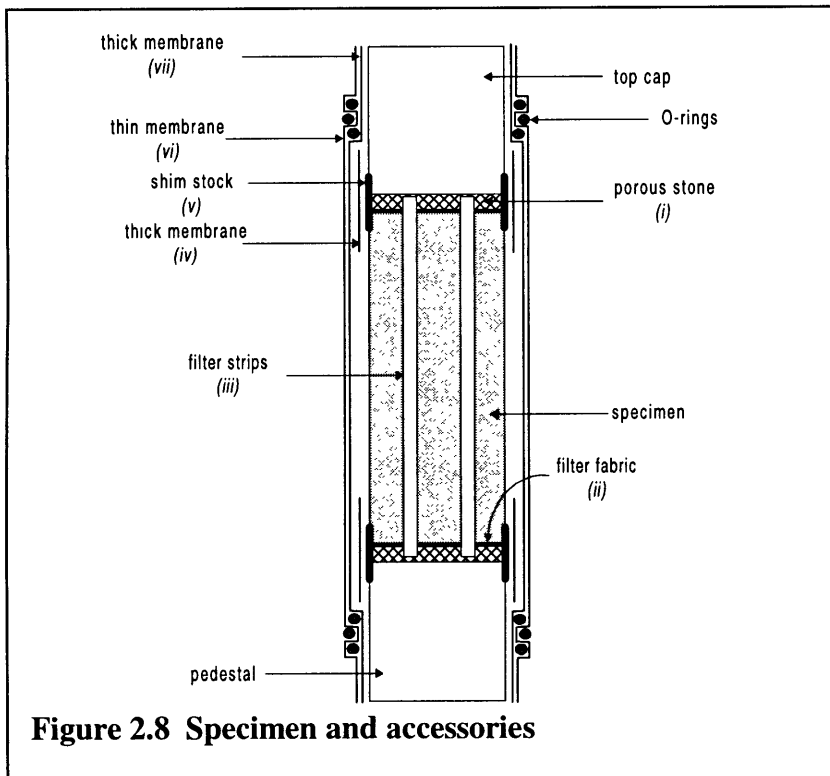


motor, pore PVC motor (Figure 2.5, *iii*). Signals are then sent out to move the motors (via a digital-to-analog interface on the motor translator) to account for the differences in stress-strain state. For example, in the specimen saturation process, a target back pressure has to be continually maintained. If the actual back pressure deviates from the target back pressure, the pore pressure PVC motor will be activated to correct for the difference.

### 2.3 Specimen Setup

Prior to setting the specimen in the triaxial cell, the height and diameter of the specimen are measured with a caliper. The average of three measurements taken at different locations is recorded. The mass of the specimen is also determined.

Figure 2.8 shows a diagram of the specimen and the necessary accessories. Due to the high swell stresses of these clay-sulfate specimens, all of the specimen setup is done dry, and the



specimen is not exposed to any water until back pressure saturation. The specimen is set on the pedestal on top of a layer of filter fabric (*ii*) (monofilament nylon) and a porous stone (*i*); similarly, a filter fabric and porous stone are placed between the specimen and the top cap. Eight strips of filter paper (*iii*)

(Whatman: 0.25" in width, 2.25"-2.75" in length) are equidistantly arranged around the specimen; the filter strips allow for easier flow of water to and from the specimen. Strips of shim stock (*v*) (Precision Brand Stainless Steel Shim; 0.001" thick, 0.5"-0.7" in width, 12" in length) are wrapped around the junctions of the specimen and the top cap, as well as that of the specimen and the pedestal. The shim strips prevent membranes from being pinched and punctured between the specimen and the pedestal/top cap under high pressures. A small strip of thick latex membrane (*iv*) (1" in width, 1.4" in diameter, 0.012" thick) covers each shim strip to prevent the edges of the shim stock from puncturing the thin membrane (*vi*). One layer of thick latex membrane (*vii*) (1.4" in diameter, 0.012" thick) is then rolled onto the specimen. Two O-rings are placed on the thick membrane at each end. One layer of thin membrane (*vi*) (Trojan Latex Condoms) is rolled over the thick membrane (*vii*). One O-ring is then placed at each end on the thin membrane and positioned snugly between the first two O-rings.

After the specimen has been set on the pedestal, the cell is filled with silicon oil (Dow Corning silicon oil: 200 Fluid, 20 cst). Air pressure is then used to fill and drain the triaxial chamber. As shown in Figure 2.6, the silicon oil flows from a pump tank (*ii*). The pump tank contains a bag filled with silicon oil and a diaphragm near the top. An air compressor (*i*) produces pressurized air that pushes on the diaphragm, which forces silicon oil out the bottom of the pump tank, through a tube, and into the triaxial chamber. To drain the cell, air pressure is applied at the top of the triaxial chamber (Figure 2.1) to force oil out and back into the pump tank. As Figure 2.6 shows, a three-way valve connects the chamber to the pump tank and to the pressure-volume controller. The valve makes it possible to isolate the chamber from the cell pressure source. The cell pressure transducer (*iii*) (Data Instruments: model AB HP, 2000psi) is located between the three-way valve and the pressure-volume controller.

Silicon oil is chosen as the confining fluid in this setup for numerous reasons. This fluid does not conduct electricity, which makes it ideal for use in the presence of electrical devices such as load cells or small strain measurement devices when used. Also, silicon oil does not penetrate the membrane, and, thus, membrane leakage is eliminated. Furthermore, silicon oil does not disintegrate membranes that enclose the specimen even over long periods of time, which is critical since typical shear tests last about a week.

## **2.4 Triaxial Testing Procedures**

Both drained and undrained shear tests were performed. As discussed in the previous chapter, shales have extremely low hydraulic conductivity; Brace (1980) cites the hydraulic conductivity of shales to be in the range of  $10^{-6}$  to  $10^{-11}$  darcy. Pore pressure redistribution occurs in small regions, and shales exhibit largely undrained mechanical response over a wide range of conditions. As a result, more time was spent on performing undrained tests in this testing program.

After the cell has been filled with silicon oil, the system is ready to be pressured-up. Pressure up, or increasing confining stress on a dry sample, is achieved through the computer's "Undrained Isotropic Initial Stress" option, which prompts for a target confining stress and axial seating load. Since the rock is dry and has no initial pore pressure, the target confining stress is the desired pre-consolidation stress; in this case, the pre-consolidation stress is between 70-90 ksc. The cell pressure is applied incrementally by the cell PVC. Simultaneously, an axial seating load of about 10 kg is applied during pressure up. At the end of pressure up, the cell pressure, axial load, axial strain, and pore pressure are recorded. The stress condition is held for 24 hours to ensure system stability.

The next step is back pressure saturation, which entails introduction of water into the specimen and applying a back pressure while preserving the initial effective stress. Using the “Drained Isotropic Stress Change” option, the back pressure and the confining pressure are simultaneously applied in increments of 2 ksc, with stress conditions held for an hour after each increment. After each increment, the cell pressure, back pressure, axial stress<sup>3</sup>, axial strain, and volumetric strain are recorded.

A B-value is obtained after every two or three increments. The “Check B-value” computer option increases the confining pressure by a designated increment, while the pore drainage lines are closed, and calculates the ratio of the change in pore pressure to the change in confining pressure:

$$B = \frac{\Delta u}{\Delta \sigma_c}$$

The B-value results will be discussed in the next chapter.

To ensure 100% saturation, a high back pressure is necessary to dissolve all of the air in the specimen. However, back pressure saturation is limited by the capacity of the instruments, specifically the motor on the PVCs. The maximum torque on these motors is the equivalent of about 105 ksc, which is therefore the upper limit for the confining stress. Thus, depending on the pre-consolidation stress, the highest attainable back pressure for each test is different and ranges from 15 ksc to 35 ksc. After the maximum back pressure has been attained, stress is held for 24 hours. During this time, the volumetric strain is monitored to see whether water continues to enter the specimen – an indication that the sample is not fully saturated yet.

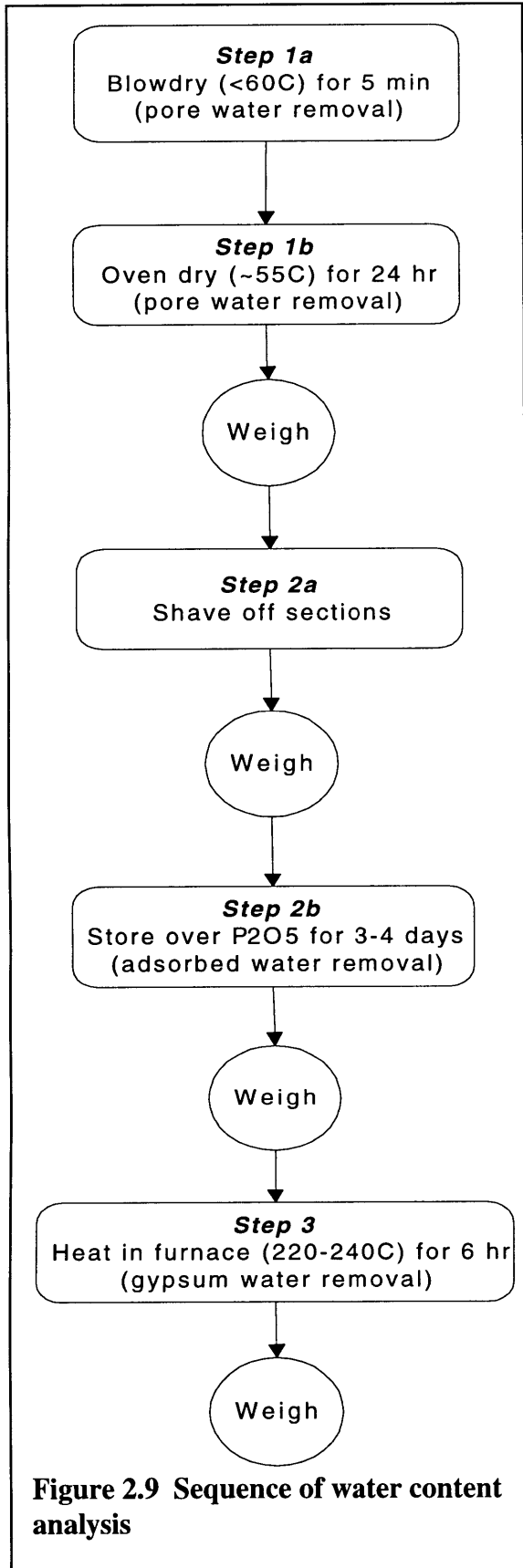
---

<sup>3</sup> The axial stress is calculated from:

$$\sigma_1 = \sigma_3 + \frac{L}{A}$$

where  $\sigma_1$  is the axial stress,  $\sigma_3$  the confining stress,  $L$  the axial load, and  $A$  the cross-sectional area of the specimen. Note: stresses are in kg/cm<sup>2</sup>, load in kg, and area in cm<sup>2</sup>.





After back pressure saturation, the specimen is ready for shear. The “Undrained Shear” option prompts for an axial strain rate and maximum axial stress. Typically, the experiments are performed at a shearing rate of 0.12%/hour, though some tests are run with different shearing rates to assess the effect of shearing rate on strength. The maximum axial stress input serves to protect the load cell from being loaded beyond its capacity and is calculated from the load cell capacity. For the Kulite 2500 lb. load cell, the capacity is assumed to be 1.5 times the reported capacity, i.e.,  $2500 \times 1.5 = 3750$  lb. Assuming that the cross-sectional area of the specimen is about  $10 \text{ cm}^2$ , the maximum deviatoric stress is 168 ksc, and the maximum axial stress is 168 ksc plus the pre-consolidation stress. During shear, the confining stress is held at the pre-consolidation stress, while the axial load is increased at the designated strain rate. The tests are terminated when 15% axial strain is achieved; in the event of instrument malfunction, the test is terminated sooner.

## 2.5 Gypsification Analysis

After the specimens are tested in the triaxial cell, they are removed from the cell and stripped of all membranes and filter materials. The mass of the wet specimen is determined. Water content analysis is then performed to quantify and characterize areas of gypsification. The following series of tests are performed to isolate the pore water, the adsorbed water, and the gypsum water. The flow chart in Figure 2.9 maps out each step of the water content analysis.

### 2.5.1 Pore Water

To remove pore water on the surface of the specimen, a blow dryer is used to gently evaporate the excess pore water for about 5 minutes. A thermometer is placed near the specimen to ensure that the temperature around the specimen stays well below 60°C, since gypsum begins transforming back to anhydrite at 58°C at atmospheric pressure (Hardie, 1967). To remove the pore water from the inner portions, the specimen is then placed in a 55°C oven for 24 hours. After removal from the oven, the specimen is cooled in a desiccator over silica gel. The cooled, dried mass is weighed, and the amount of pore water is quantified using the wet and dried mass of the specimen. The pore water content  $w_{C_{pore}}$  is calculated from the following formula:

$$w_{C_{pore}} = \frac{m_{wet} - m_{55C}}{m_{55C}}$$

where  $m_{wet}$  is the mass of the wet specimen and  $m_{55C}$  is the mass of the specimen after being heated in the oven at 55°C.

### 2.5.2 Adsorbed Water

In conventional water content analysis of clays, adsorbed water is removed by heating the material at 105°C for 24 hours. However, the conventional method cannot be used for this study, because gypsification begins to reverse at 58°C. If adsorbed water is to be distinguished from gypsum water, the adsorbed water in the specimen must be removed through some other means.

In an alternative method, sections of the oven-dried specimen are shaved off with a razor blade and placed in a dessicator over phosphorous pentoxide ( $P_2O_5$ ). After 3-4 days in the dessicator,

$$WC_{ads} = \frac{m_{samp} - m_{P2O5}}{m_{P2O5}}$$

the material is weighed, and the percentage of adsorbed water is determined. The adsorbed water content  $wc_{ads}$  is determined from:

where  $m_{samp}$  is the mass of the shaved samples and  $m_{P2O5}$  is the mass of the samples after sitting over  $P_2O_5$  for 3-4 days.

### 2.5.3 Gypsum Water

In the final stage of the water removal process, the material is heated in a 220-240°C furnace for 6 hours. After cooling in a dessicator over silica gel, the final mass of the material and the percentage of gypsum water are determined. Similar to the water contents calculated above, the gypsum water content  $wc_{gyp}$  is obtained from:

$$WC_{gyp} = \frac{m_{P2O5} - m_{220C}}{m_{220C}}$$

where  $m_{220C}$  is the mass of the sample after being heated in the furnace.



### 3 Data Analysis

#### 3.1 Triaxial Test Results

Tables 3.1 and 3.2 list the different tests that were performed in this testing program. Of the eleven tests that were performed, nine were unconsolidated and sheared in undrained compression (UUC) and two were unconsolidated and sheared in drained compression (UDC). A series of six UUC tests were sheared at the same rate but performed under different pre-consolidation stresses ranging from 50 ksc – 90 ksc; multiple tests were performed with the same pre-consolidation stress to assess reproducibility of the results. Three of the UUC tests --TX423, TX425, TX426 -- involved varying the shearing rate without changing the pre-consolidation stress.

##### 3.1.1 Stress Paths

Figures 3.1 and 3.2 show typical stress paths for the UUC and UDC tests, respectively. Stress paths are depicted in p-q space, where p represents the mean stress and q the deviatoric stress. The definitions of p and q are as follows:

$$p = \frac{\sigma_v + \sigma_h}{2} \quad q = \frac{\sigma_v - \sigma_h}{2} \quad p' = \frac{\sigma'_v + \sigma'_h}{2} \quad \text{Equation 3.1a,b,c}$$

where  $\sigma_v$  and  $\sigma_h$  are the vertical and horizontal stresses, respectively; the apostrophes (') denote effective stresses. As noted in the legends, the total stress paths (TSP) are marked by open symbols, while the effective stress paths (ESP) are indicated by shaded symbols. Effective stress paths are calculated by subtracting the pore pressure from the total stress path at any stage in the shearing process, i.e.  $\sigma' = \sigma - u$  and  $p' = p - u$ , where  $u$  is the pore pressure. For UUC tests, the excess pore pressure  $\Delta u$  can be calculated from

$$\Delta u = p - p' - u_o, \quad \text{Equation 3.2}$$

<b>Undrained</b>									
<b>Test Number</b>	<b>TX391</b>	<b>TX411</b>	<b>TX413</b>	<b>TX415</b>	<b>TX423</b>	<b>TX425</b>	<b>TX426</b>	<b>TX429</b>	<b>TX430</b>
$\sigma'_{co}$ (ksc)	50	80	80	90	90	90	90	70	70
Strain Rate (%/hr)		0.13	0.14	0.12	0.09	0.05	0.62	0.12	0.12
<b>at failure...</b>									
Normalized Shear Strength	0.792	0.504	0.565	0.543	0.567	0.576	0.629	0.631	0.636
Friction Angle (degrees)	27.9	24.6	22.51	22.69	23.789	23.28	23.34	24.32	23.92
Shear Strain(%)	6.83	7.69	11.30	7.88	2.45	0.89	9.62	10.50	9.02
A-parameter	0.020	0.285	0.069	0.116	0.135	0.095	0.025	0.078	0.043
Normalized Excess Pore Pressure	0.029	0.283	0.077	0.124	0.151	0.108	0.030	0.096	0.054
Failure Mode	Shear plane	shear plane	shear plane	shear plane	bulge	bulge	shear plane	shear plane	shear plane

**Table 3.1 Summary of undrained tests**

<b>Drained</b>		
<b>Test Number</b>	<b>TX404</b>	<b>TX407</b>
$\sigma'_{co}$ (ksc)	50	70
Strain Rate (%/hr)	0.08	0.03/0.13 <sup>4</sup>
<b>at failure...</b>		
Normalized Shear Strength	0.544	0.596
Friction Angle (degrees)	26.2	29.7
Shear Strain(%)	4.79	6.76
Failure Mode	shear plane	bulge

**Table 3.2 Summary of drained tests**

<sup>4</sup> Due to instrumentation mishap, the strain rate was 0.03%/hr for the first half of the test and 0.13%/hr for the last half of the test.

where  $u_0$  is the pre-shearing pore pressure. Graphically, Equation 3.2 superimposes the total stress path onto the effective stress path, and the difference is the excess pore pressure.

The stress paths in Figure 3.1 indicate that specimens sheared undrained in compression develop positive pore pressures. As the shearing progresses, specimens tend to dilate, which causes a slight decrease in positive pore pressure. After the specimen has failed, the pore pressure increases again.

In UUC tests, excess pore pressures are generated during shear. Figure 3.3 shows the

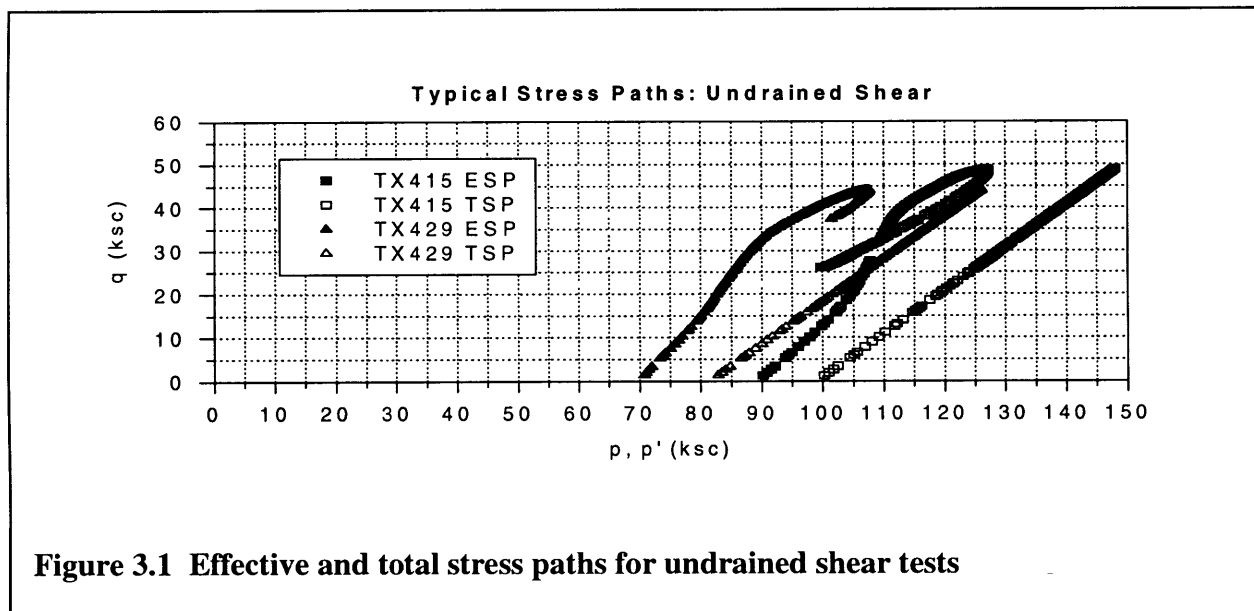


**Figure 3.1** Effective and total stress paths for undrained shear tests

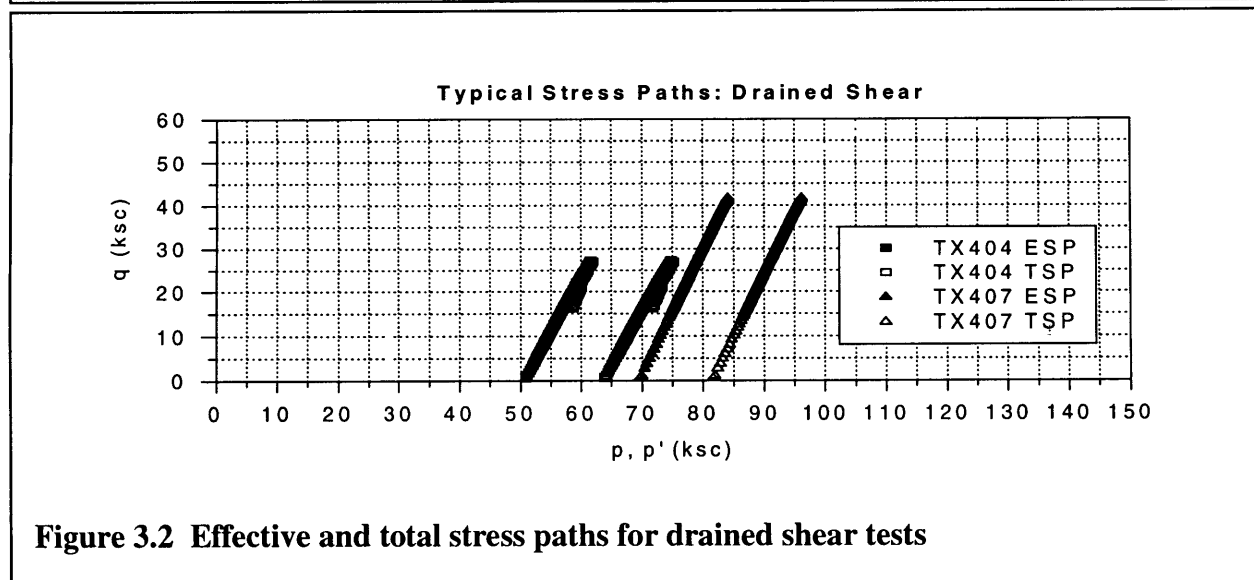
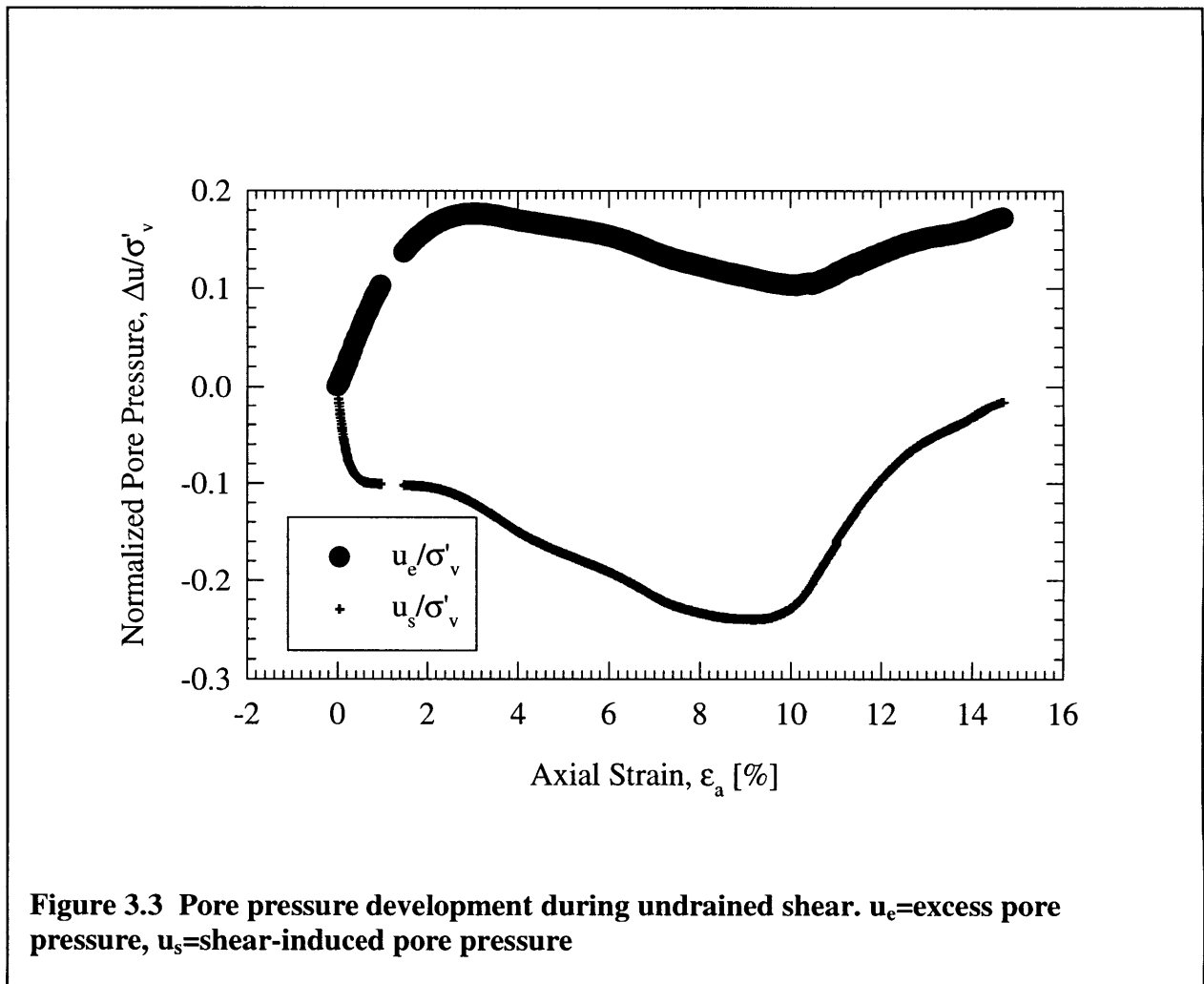


**Figure 3.2** Effective and total stress paths for drained shear tests

development of the excess pore pressure versus axial strain and shows the same trends as the stress paths in Figure 3.1. There are two sources of excess pore pressure: changes in octahedral stress and changes in deviatoric stress. In tests that follow a pure shear stress path, there is no change in octahedral stress. Therefore, all excess pore pressures generated in pure shear tests are shear-induced. The tests presented in this paper are conventional triaxial compression tests, where the octahedral stress is not constant. In conventional triaxial compression tests, the shear-induced excess pore pressure can be calculated by subtracting the change in octahedral stress from the excess pore pressure.

Figure 3.2 shows the stress paths for the two drained tests. As expected, the shapes of the





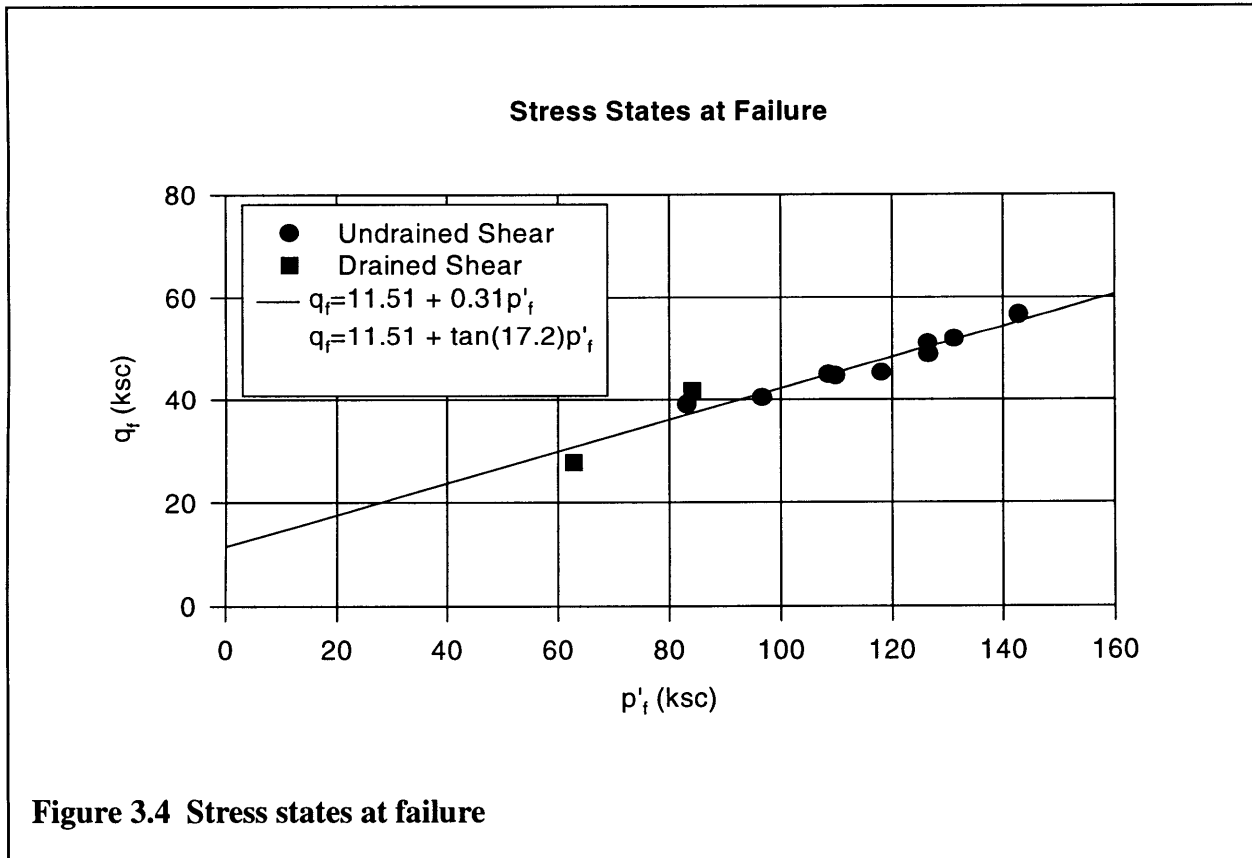
ESP and TSP are similar, because any excess pore pressure developed during shearing is allowed to dissipate through the pore drainage lines (Figure 2.1).

### 3.2 Shear Strength

The stress states at failure for the eleven tests are shown in Figure 3.4. The results suggest that shear strength generally increase with mean effective stress. The data are fitted through a straight line that represents the average failure envelope. The intercept and slope of the line determine the average cohesion and friction angle, respectively: the average cohesion  $a$  is 11.51 ksc and the average friction angle  $\alpha$  is 17.2°.

Since the specimens are reconstituted, the maximum past pressure and the overconsolidation ratio (OCR) can be calculated. The overconsolidation ratio is defined as:

$$OCR = \frac{\sigma'_{v \max}}{\sigma'_{vc}} \quad \text{Equation 3.3}$$



where  $\sigma'_{vmax}$  is the maximum past vertical effective stress and  $\sigma'_{vc}$  the vertical effective consolidation stress. The conventional definition of OCR is with reference to  $K_0$ -consolidation; the specimens in this testing program were produced under hydrostatic conditions. Thus, the value calculated for these specimens is an apparent OCR. For the specimens used in this study,  $\sigma'_{vmax}$  is 100 MPa (1000 ksc) -- the pressure used to solidify the powder mixture into specimens (see section 2.1.1). According to Equation 3.3, the specimens in this testing program have an apparent OCR of 10-20.

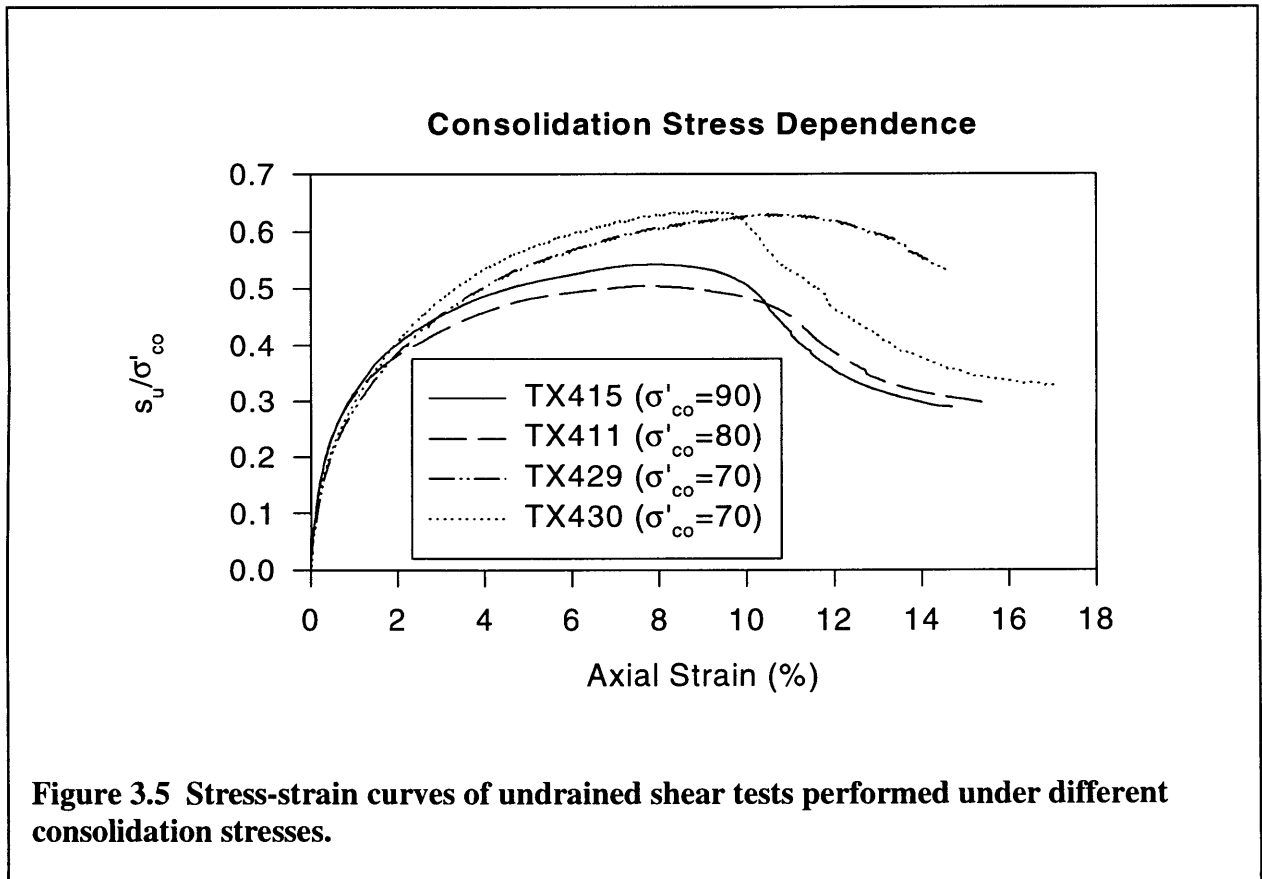
The normalized undrained shear strength for these clay-sulfate specimens range from 0.504-0.792. In comparison to naturally occurring clayey rocks, clay-sulfate rock of this composition has unusually low strength. For example, Opalinus shale of OCR=14 exhibits normalized shear strength that range from 2.0-2.5 (Aristorenas, 1992). According to the SHANSEP model used in Figure 1.7, naturally occurring shale of OCR=10-20 are expected to exhibit normalized undrained shear strength between 2.0-3.0. Or, conversely, naturally occurring shale that show an normalized undrained shear strength of 0.5-0.8 is expected to have OCR=2-3. When applied to SHANSEP, the strength data suggests that the mechanical overconsolidation of these clay-sulfate specimens is not entirely locked in. Another words, clay-sulfate rocks of this composition have no “memory” of the maximum past pressure and behave as if they had an OCR=2-3. This effect may be due to the composition of the material. SHANSEP describes the behavior of normally to slightly overconsolidated clays. The clay-sulfate specimens used in this testing program are predominantly anhydrite (85%), which may result in mechanical behavior different from that of clay.

### **3.2.1 Stress-Strain Curves**

Figures 3.5 and 3.6 show the stress-strain curves for undrained tests. The shear stress is

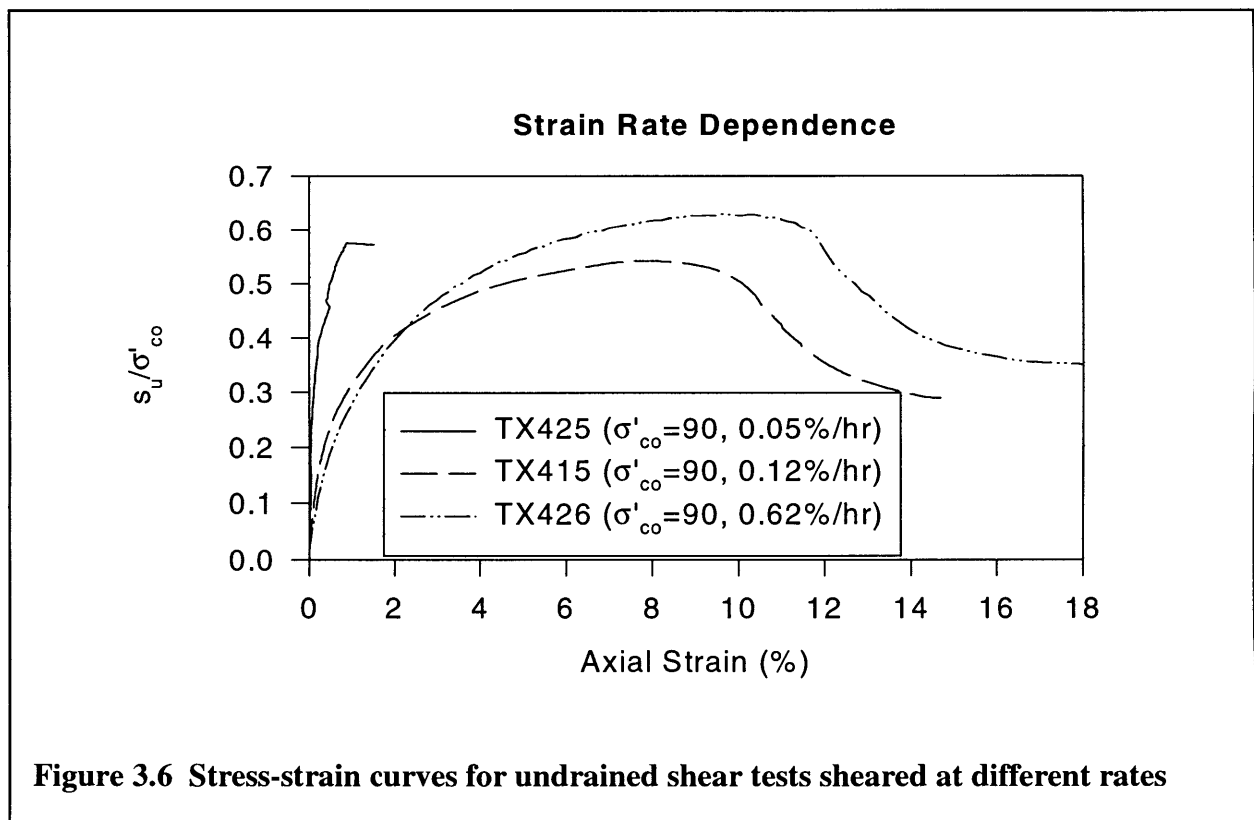
denoted by  $s_u$ , which is defined as  $(\sigma_v - \sigma_h)/2$ ; in the stress-strain plots the shear stress is normalized to the respective consolidation stress. The axial strain is calculated from the displacement of the axial DCDT, which monitors the movement of the loading piston. The shapes of stress-strain curves for most tests, regardless of consolidation stress or strain rate, are similar. As shearing progresses, the shear stress increases, with a decreasing slope. The specimens reach peak strength and then show a drop in strength as shearing continues.

Figure 3.5 shows the stress-strain curves for undrained tests sheared at the same rate ( $\sim 0.12\%/hr$ ) but conducted under different consolidation stresses. For clays, it has been observed that the shape of the stress-strain curve is dependent on the consolidation stress. Specifically, at low confining stresses, the specimen has higher strength and fails at lower strain, while higher confining stresses results in the opposite. Evidently, clay-sulfate rocks exhibit a



similar behavior. Figure 3.5 shows that the tests conducted at 70 ksc had higher normalized strength than those conducted at 80 and 90 ksc. The curves for 80 and 90 ksc do not follow the trend, which may be due to specimen variability. With such high apparent OCR=10-20, a difference of 20 ksc in confining stress is most likely not enough to not produce very different stress-strain curves for these clay-sulfate specimens. The fact that the 70 ksc tests are separate from the 80 and 90 ksc tests suggests that there may be some correlation. In order to confirm this relationship, more tests need to be performed over a wider range of confining stresses.

The stress-strain behavior also exhibits a possible dependence on strain rate. Figure 3.6 compares the normalized stress-strain curves of TX425, TX415, TX426 which were sheared at 0.05%/hr, 0.12%/hr, and 0.62%/hr, respectively. In comparing the two tests performed at the higher strain rates, the general shapes of the two stress-strain curves are similar, but there appears to be a shift in both the x- and y-directions. Specifically, the higher shearing rate causes



the specimen to fail at higher strain with higher peak strength. The test sheared at the lowest strain rate (TX425), failed at significantly lower strain but had an intermediate peak strength. Though these data suggest a strong influence of strain rate on stress-strain curves, more tests at other strain rates need to be performed to confirm this relationship.

### 3.2.2 *B-values*

The Skempton pore pressure parameter B (or B-value) is the ratio of the excess pore pressure increment and the isotropic stress increment applied during undrained stress loading or unloading. The B-value has been traditionally used to assess the degree of saturation of a test specimen. For fully saturated soil specimens, the B-value approaches unity. If the specimen is not fully saturated, the isotropic increase (or decrease) in confining stress will be taken on by compressible air bubbles in the specimen instead of the pore fluid, in which case the B-value will be significantly less than one. In a sample saturated using back pressure saturation, all air bubbles are dissolved by the back pressure. The B-value is higher for saturated samples; since there are no air bubbles present, the nearly incompressible pore fluid generates pressure when the specimen is isotropically stressed. In traditional soil testing, specimens are usually not consolidated or sheared until the B-value is close to one (i.e., greater than 0.97).

Fully saturated rocks and stiff sands can yield B-values significantly less than one. This is because the B-value is a function of compressibilities of the skeleton, the fluid constituent, the solid constituent, as well as the porosity. Based on Biot's poroelastic theory, the pore pressure parameter B can be expressed as:

$$B = \frac{\frac{1}{K} - \frac{1}{K_s}}{\frac{n}{K_f} - \frac{n}{K_s} + \frac{1}{K} - \frac{1}{K_s}} \quad \text{Equation 3.4}$$

where  $n$  is the porosity, and  $K$ ,  $K_s$ , and  $K_f$  are the bulk moduli of the skeleton, the solid constituent, and the fluid constituent, respectively. For most soils,  $K$  is significantly smaller than  $K_s$  and  $K_f$ . Therefore,  $B$ -value for soils is pretty close to one. For stiff materials, such as rocks,  $K$  may be comparable to  $K_s$  and  $K_f$ , resulting in  $B$ -values of less than one.

In this testing program, the  $B$ -values measured for saturated clay-sulfate rock range from 0.30-0.45. To assess whether such low  $B$ -values are reasonable, the theoretical  $B$ -value of clay-sulfate rocks will be calculated using Equation 3.4. Typical constituent bulk moduli will be used in this calculation:  $K_f=2.18 \times 10^3$  MPa for water,  $K_s=1.00 \times 10^4$  MPa (Aristorenas, 1992). The porosity for clay-sulfate rock, obtained from phase relations, is about  $n=0.28$ . The bulk modulus of the skeleton is obtained from the expression:

$$K = \frac{2G(1+\nu)}{3(1-2\nu)} \quad \text{Equation 3.5}$$

where  $G$  is the shear modulus at small strains and  $\nu$  is the drained Poisson's ratio, assumed to be  $\nu=0.4$ . The modulus  $G$  is obtained from drained shear results and estimated to be about 18000 ksc or  $1.8 \times 10^3$  MPa. Hence, the bulk modulus of the skeleton is  $K=8.4 \times 10^3$  MPa. Substituting the appropriate values in Equation 3.4, a theoretical  $B$ -value of about 0.44 is obtained. Hence, the low  $B$ -values measured for clay-sulfate specimens are reasonable for saturated stiff materials.

### 3.2.3 Modes of Failure

The clay-sulfate rock specimens fail in one of two modes. Most of the specimens fail with a single shear plane, while others are bulged; the failure modes found in each test are listed in Tables 3.1 and 3.2. According to the stress-strain curves of bulged specimens, strength increases with strain and plateaus at the maximum strength, which is a behavior typical of ductile material. Ductile specimens bulge into a barrel shape very similar to that of clay sheared to

failure. Figure 3.7 shows the failure mode of the ductile specimens and the corresponding stress-strain curve.

Brittle specimens form one or more shear planes at failure. For the specimens that fail with a shear plane, stress increases with increasing strain, reaches peak strength, and decreases after failure. There is typically one major shear plane, with some minor fractures branching off the shear plane near the ends of the specimen. The angle  $\alpha$ , as defined in Figure 3.8, ranges from  $54^{\circ}$ - $60^{\circ}$ .

Whether a specimen exhibits ductile or brittle failure typically depends on the confining stress and strain rate. Specifically, brittle behavior dominates at low confining stress and faster shearing rate, and ductile behavior prevails at high confining stress and slow shearing rate. The data from this testing program are generally consistent with the theory described above, as far as strain rate is concerned. The four tests in Table 3.1 that are shaded gray were all conducted under a confining stress of 90 ksc. Of these four tests, the two sheared at higher rates showed brittle behavior, while the two sheared at slower rates showed ductile behavior. Thus, holding confining stress constant, one can conclude that clay-sulfate rocks exhibit brittle behavior when sheared at relatively high rates and ductile behavior when sheared at low rates.

In the two drained tests (Table 3.2), the test with the higher confining stress failed in bulging, which suggests that higher confining stresses lead to ductile behavior. The undrained tests, however, do not show correlation between confining stress and failure mode at constant strain rate, at least for confining stresses ranging from 50-90 ksc. In order to draw conclusions on the relationship between confining stress and failure mode, more tests need to be performed over a wider range of confining stresses.

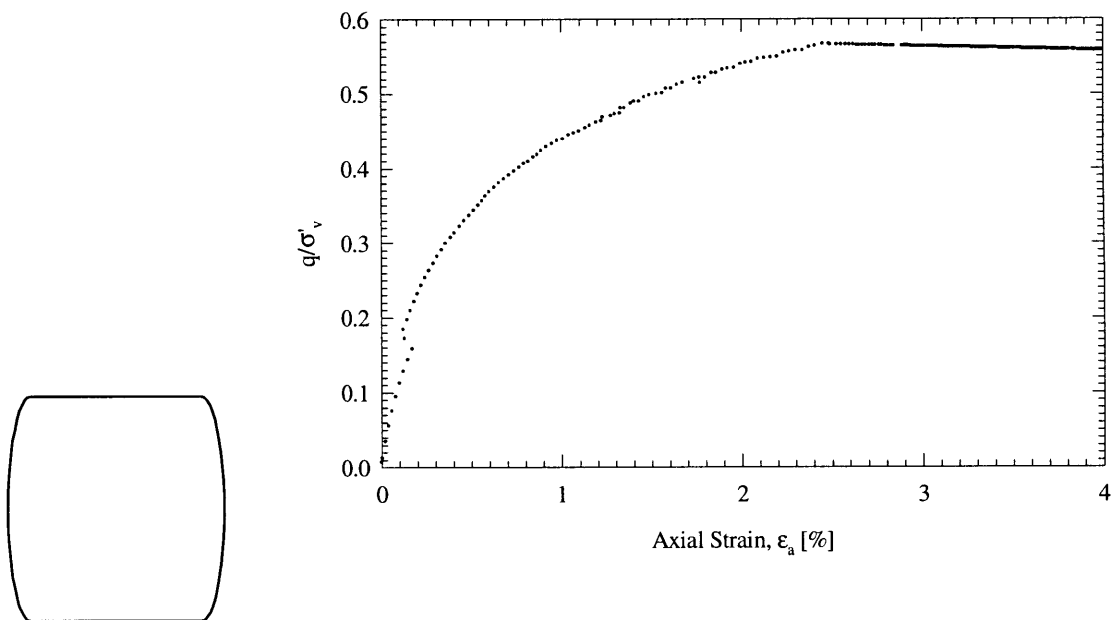


**Figure 3.7 Ductile failure with corresponding stress-strain curve**

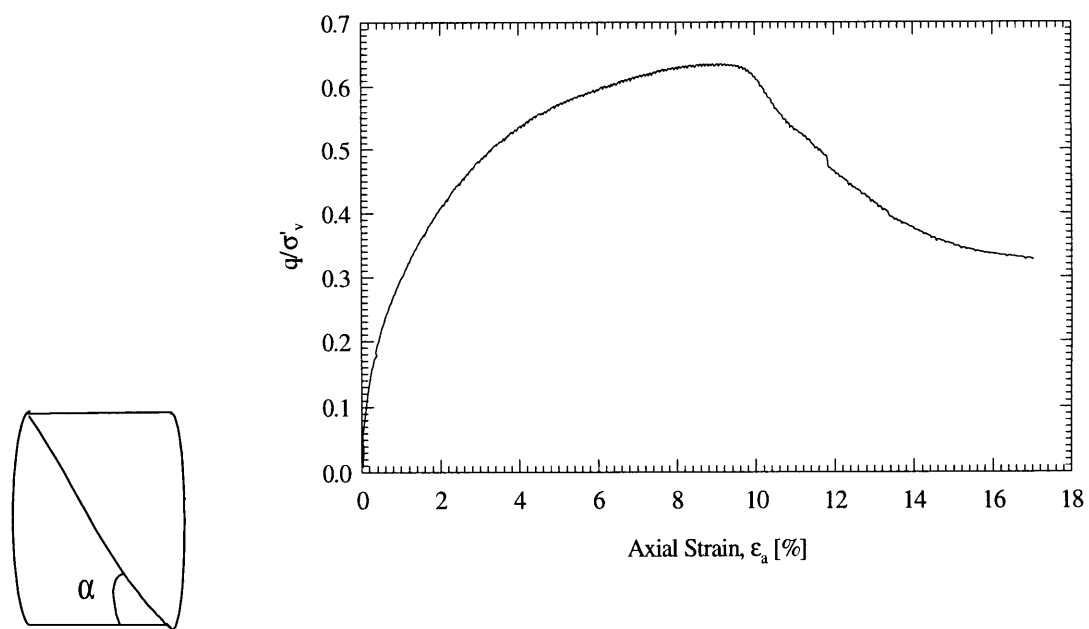


**Figure 3.8 Brittle failure with corresponding stress-strain curve.**



### 3.3 Gypsification Analysis

The purpose of the second half of the testing program is to determine the effect of shear on gypsification in the specimens. Since gypsification is a chemical reaction that attaches water molecules onto anhydrite, water contents are used to assess the extent of gypsification. This is done by reversing the gypsification process and by recording the amount of gypsum water that is removed in the reversal process. From the amount of gypsum water removed, a measure of gypsification is obtained.

“Gypsum” water refers to that involved in the gypsification reaction only. As described in the previous chapter, water that enters the specimen ends up in one of three places: pore space (pore water), clay mineral surface (adsorbed or clay water), anhydrite transformation (gypsum water). Thus, to measure the amount of gypsum water, the gypsum water has to be isolated from the pore and clay water. The procedure, as described in Chapter 2, is to remove the pore and clay water first and the gypsum water last.

Shearing in clay-sulfate rocks is expected to increase gypsification in two ways. First, the intensity of the shearing causes surfaces to scrape against each other and results in cracking of gypsum crusts. Cracking exposes more anhydrite surfaces to water and enhances gypsification. Secondly, shearing of brittle material such as shales tend to cause dilation in the shear zone, which is the rearrangement of grains resulting in an increase of pore space. By increasing the pore space and, consequently, generating negative pore pressures, dilation draws more water into the shear zone and makes the area more conducive to gypsification. Thus, due to these shear-induced mechanisms, gypsum levels are expected to be higher in sheared specimens, particularly in the shear plane.

### 3.3.1 Water Distribution

Due to the low hydraulic conductivity of clay-sulfate rocks, there was concern as to whether water actually enters the center of the specimen. A water distribution test was performed on a saturated, but unsheared specimen. After the specimen was removed from the chamber, it was divided into five relatively even disks, around 1 cm thick. Pore, adsorbed, and gypsum water content of each disk was obtained. As Table 3.3 shows, the water contents in the different sections show no decreasing trend towards the center of the specimen, as would be expected if water is unable to permeate the specimen. With the exception of the high pore water content in disk 4, the results show fairly consistent water contents throughout the specimen, without particularly higher values at the ends of the specimen. Figure 3.9 is the contour version of Table 3.3; blank areas in the contours indicate areas of homogenous water content.

		Water Content (%)		
	Disk	Pore	Adsorbed	Gypsum
Top	1	0.1368	0.0105	0.0045
	2	0.1362	0.0104	0.0038
	3	0.1378	0.0108	0.0039
	4	0.1753	0.0105	0.0033
Bottom	5	0.1288	0.0105	0.0036

**Table 3.3 Water content distribution throughout specimen; “Top” refers to top of specimen, and “Bottom” the bottom end of specimen.**

### 3.3.2 Effectiveness of $P_2O_5$

Another concern regarding using water content analysis to determine gypsification is the effectiveness of phosphorous pentoxide ( $P_2O_5$ ) as a means of removing adsorbed water from the clay minerals. Thus, a test was conducted to compare adsorbed water removal using  $P_2O_5$  versus heating in a 105°C oven, which is the conventional method used to remove adsorbed water (see section 2.5.2). These tests were performed on samples from untested specimens. Since untested

samples are “dry” with respect to pore water and there should be negligible amounts of gypsum water, the only water in the samples is that adsorbed from the humidity in the air.

There are two procedures used in this test: in Method 1, two samples are baked in a 105°C oven for 24 hours, while another two are placed over P<sub>2</sub>O<sub>5</sub> for 4 days. The adsorbed water contents are then calculated from the mass of water removed from each sample. Though gypsification should not occur in the specimens, there may be some existing gypsum in the powders that were used to make these specimens. Thus, Method 2 begins by baking samples in a 220°C oven for 6 hours to remove any existing gypsum in the material. Then, the samples are exposed to room temperature and humidity for a week. During the week, water from the air humidity is adsorbed onto the clay minerals. Sample mass is recorded regularly during the week, and the data shows that, at the end of the

week, sample mass is relatively constant. The procedure from here on is the same as that for Method 1: half of the sample is baked in a 105°C oven for 24 hours, while the other half is placed over P<sub>2</sub>O<sub>5</sub> for 4 days.

	Method 1	Method 2
Baking	0.0146	0.0066
	0.0163	0.0056
P2O5	0.0149	0.0070
	0.0148	0.0062

**Table 3.4 Adsorbed water content results that compare adsorbed water removal by P<sub>2</sub>O<sub>5</sub> and by heat.**

Table 3.4 shows the water content results from both versions of the test. A total of eight two-gram samples were used. In comparing the two methods, Method 1 shows substantially more adsorbed water than Method 2. The mineral sheets may have collapsed during baking (220°C) in Method 2. With collapsed layers, water molecules can still adsorb onto the exterior surfaces of the layers but cannot adsorb onto the interlayer surfaces. Comparison of P<sub>2</sub>O<sub>5</sub> versus baking in 105°C shows that the amount of water removed by P<sub>2</sub>O<sub>5</sub> is comparable to that removed

### Water Distribution Contours

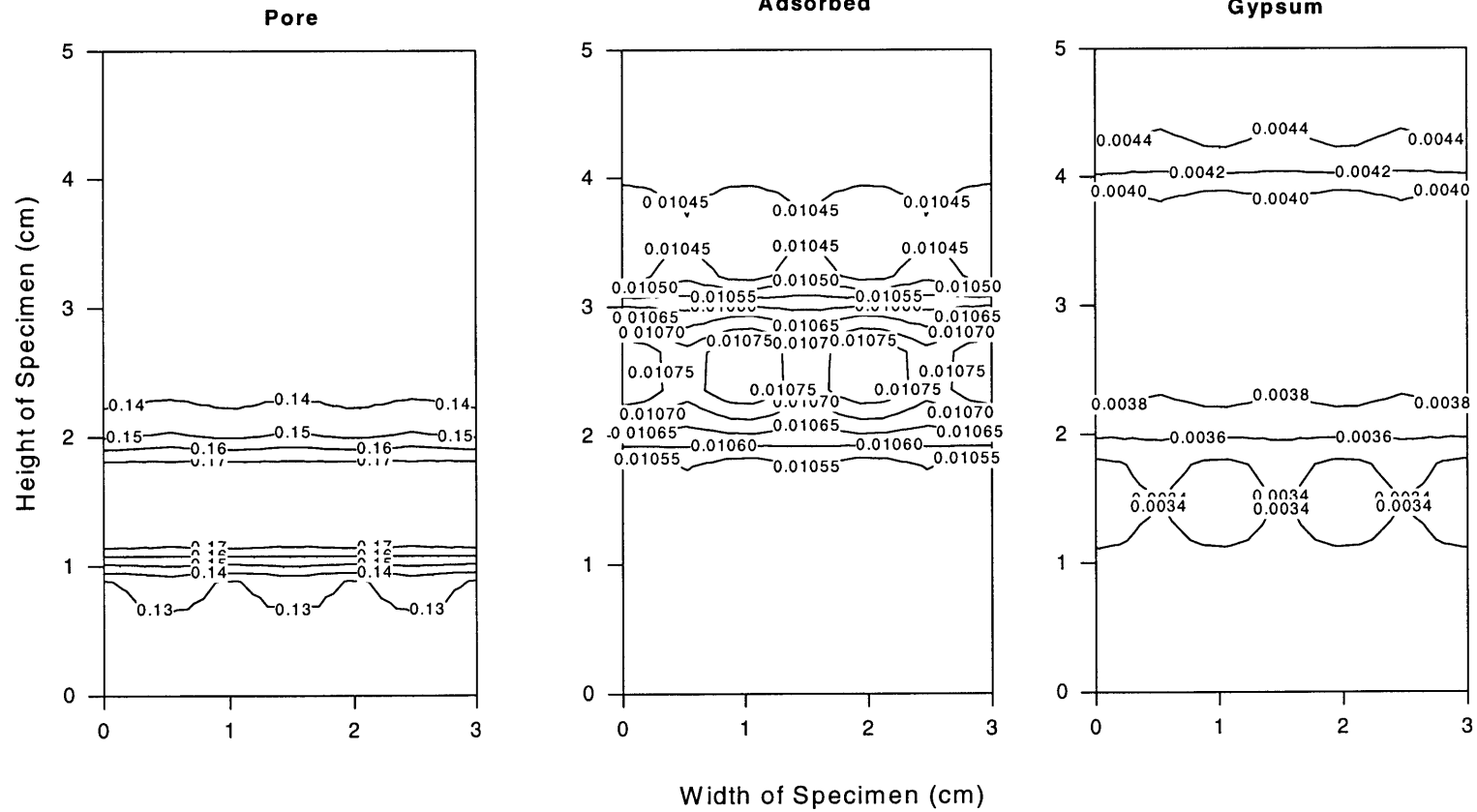


**Figure 3.9 Water distribution contours throughout specimen after back pressure saturation. Blank areas indicate homogenous water content.**

by heat for both methods. Hence,  $P_2O_5$  is an appropriate means of adsorbed water removal.

### 3.3.3 Adsorption and Gypsification Contours

After water contents have been obtained, contours of water content distribution are produced. The contours show that specimens that bulge and those that fail with shear planes have different gypsification patterns.

To obtain the contours, bulged specimens are manually cleaved, parallel to the  $\sigma_1$  axis, into a half cylinder like the one in Figure 3.10. Two millimeter sections of the sample are then shaved off in the sequence indicated by the numbers in Figure 3.10, i.e. 2 mm are

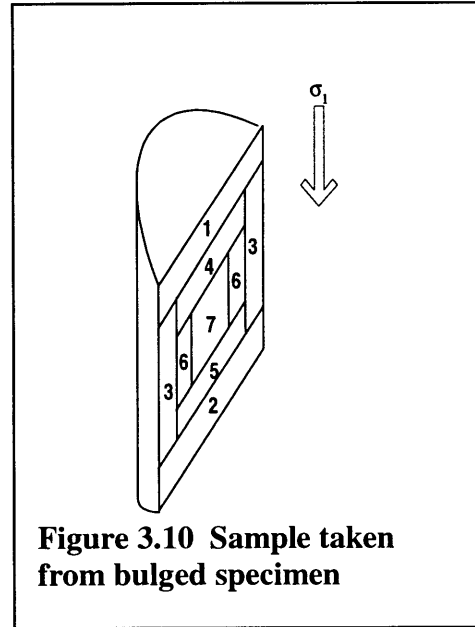


**Figure 3.10 Sample taken from bulged specimen**

shaved off the top, then the bottom, then the outer radial perimeter of the sample, and etc. Figure 3.11 shows the water content contours for TX425 of the rectangular, cross-section in Figure 3.10. The numbers on the axes are not in any metric unit and do not correspond to those in Figure 3.10. To obtain the contours, the height and width are divided into seven sections, and the numbers on the axes refer to these sections. For the purposes of this study, the trend, more so than the exact location, of gypsification levels throughout the specimen is of interest.

The gypsification contour for the bulged specimen indicates fairly uniform gypsum levels throughout most of the specimen, with slightly higher levels at the boundaries. This suggests that for specimens that exhibit ductile behavior, shearing does not appear to enhance gypsification in any particular area. The cause of high gypsification levels at the boundaries of the specimens is unknown and warrants further study.

The magnitude of the gypsification levels for TX425 appears to be unusually low.

### TX425: Undrained Shear

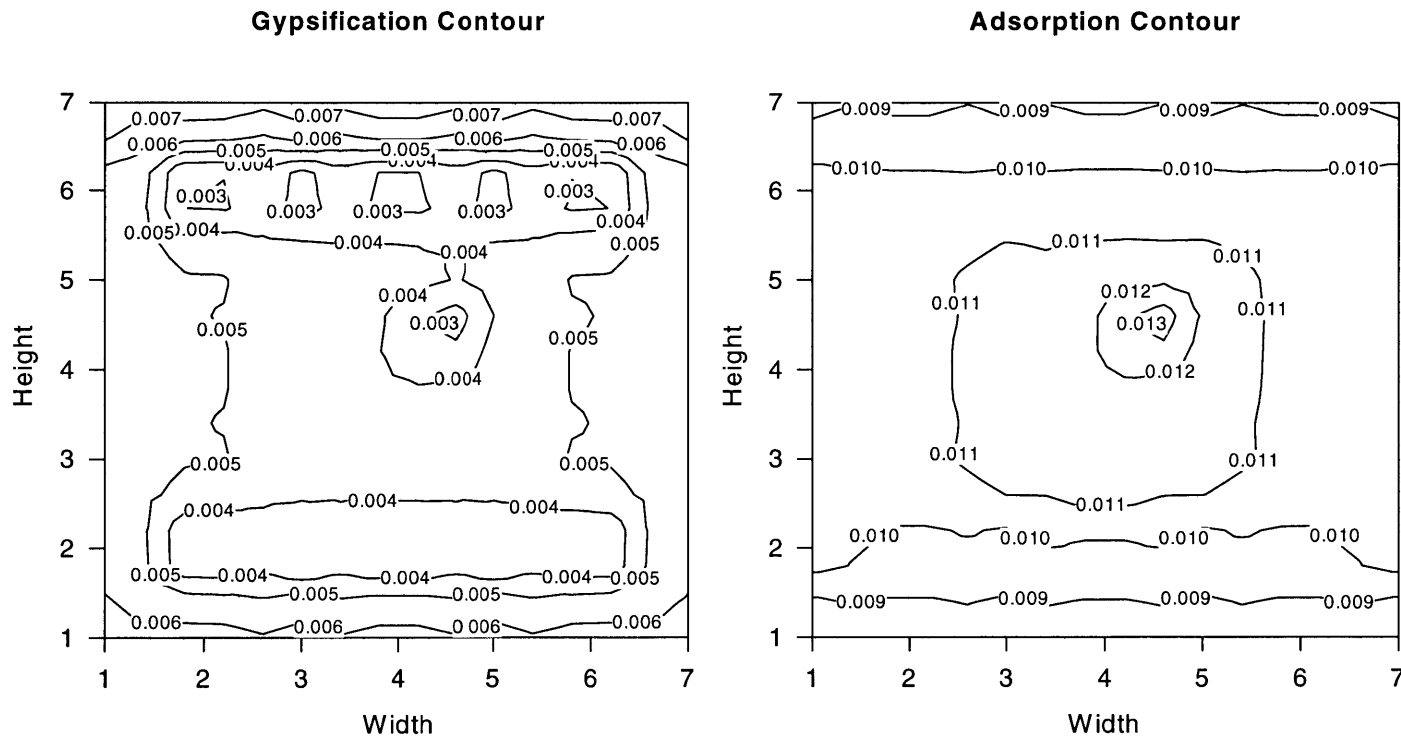


Figure 3.11 Gypsification and adsorption contour for a bulging specimen. Contours represent the rectangular cross-section show in Figure 3.10.

In fact, they are not much higher than those for the back saturated specimen, according to Table 3.5. The data from TX 423 (and other tests) suggest that 1-2% are typical gypsification levels for saturated, sheared specimens; in comparison, the water contents in TX425 are 1/3 to 1/2 of the norm. This may be due to experimental uncertainties in temperature control. Specifically, temperatures of higher than 58°C in the pore water removal process may lead to partial removal of the gypsum water, especially since the duration of the pore water removal process is 24 hours.

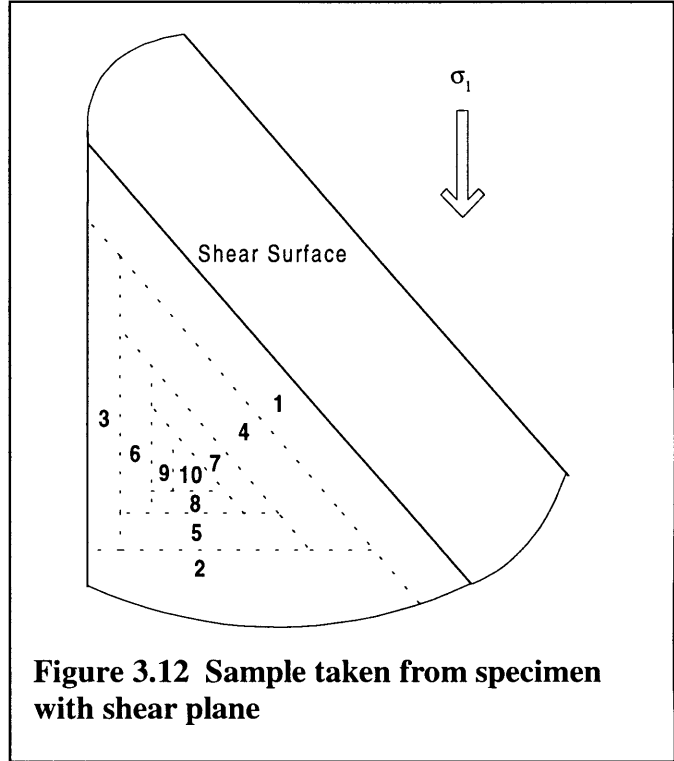
The adsorption contour for the bulged specimen shows a trend opposite that of the gypsification contour. Specifically, Figure 3.11 shows maximum adsorption in the center of the specimen and decreasing adsorption towards the edges of the specimen. As Table 3.5 shows, the adsorption levels for TX425 are comparable to those for TX423 and those for back saturated specimens. Hence, shearing does not appear to increase water adsorption in these ductile specimens.

Due to shear, the specimens that fail with shear plane naturally split into two pieces along the shear plane. One piece is cleaved parallel to  $\sigma_1$ , resulting in the shape shown in Figure 3.12. Again, the numbers in Figure 3.12 indicate the order in which the 2 mm samples were shaved. Figure 3.13 shows the corresponding adsorption and gypsification contours for TX 426. The contours represent the triangular cross-section shown in Figure 3.12.

Similar to the ductile specimen, the gypsification contour for the brittle specimen also shows high gypsification levels on the boundaries. The most interesting finding is the high gypsification level along the shear plane. This is consistent with the shear-induced gypsification described earlier. The intensity of shearing may cause particles or surfaces to scrape against each other and produce cracking of gypsum crusts that expose more anhydrite surfaces to water. The intensity of shearing is an overall effect that increases gypsification throughout the

specimen. Dilation occurs specifically in the shear zone, thereby causing the gypsum levels there to be unusually high. Dilation creates negative pore pressures in the shear zone that draw water in and, thus, increases gypsification.

As in the results from the bulged specimen, the adsorption contour for TX426 shows higher levels in the center and decreasing levels towards the perimeter – a trend opposite that of the



gypsification contours, which showed higher levels in the perimeter and decreasing levels towards the center. According to Table 3.5, the adsorbed water contents for this test are amongst the lowest observed. The low adsorbed water content is probably due to specimen variability, (i.e. lower clay/anhydrite ratio) and most likely not due to shear.

Type of Specimen	Pore	Water Contents (%)	
		Adsorbed	Gypsum
Dry	NA	1.15-1.50 <sup>1</sup>	0.83-0.99 <sup>2</sup>
back saturated	12.8-13.7	1.04-1.08	0.33-0.45 <sup>2</sup>
bulged--TX423 (no contour)	10.8	0.89-1.01	1.1-2.4
bulged--TX425 (Figure 11)	12.1	0.99-1.36	0.3-0.7
shear plane--TX426 (Figure 13)	12.3	0.67-0.93	2.0-4.0

<sup>1</sup>The specimen was not treated for pore water removal. Hence this is a combination of pore and adsorbed water content

<sup>2</sup>The data shows lower gypsum water content for a back saturated sample than for a dry sample. This may be due to variability in pre-existing gypsum content of the original anhydrite powders.

**Table 3.5 Summary of Water Content Analyses**



TX 426: Undrained Shear

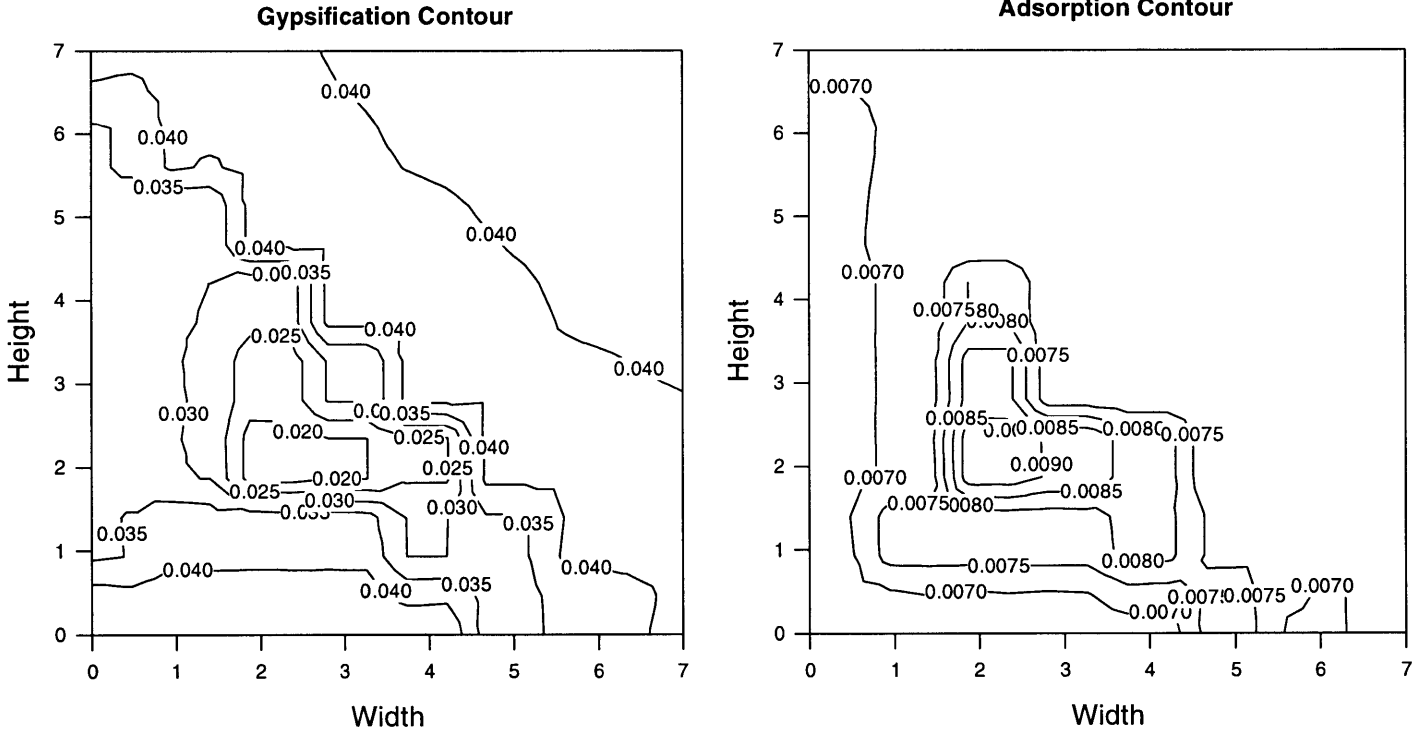


Figure 3.13 Gypsification and adsorption contour for specimen with shear plane. Contours represent the triangular cross-section shown in Figure 3.12.



## 4 Conclusion

The purpose of this work is to study the swelling behavior of clay-sulfate rocks. Clay-sulfate rocks are known to swell more than clay rocks, in terms of both severity and duration. Though the swelling of clay rocks is well understood, the chemical change involved in sulfate swelling complicates the overall swelling behavior of clay-sulfate rocks. Specifically, the hydration of anhydrite requires sufficient pore space and water. Dilation, caused by shear, draws water into the shear zone and, thus, enhances the hydration process. Therefore, the swelling of clay-sulfate rock may be induced by reduction in octahedral stress *and* by an increase in deviatoric stress. In this context, the behavior of the material is characterized through triaxial testing. Furthermore, the influence of shearing on the extent of gypsification in clay-sulfate rock is explored through water content analyses.

The specimens used in this testing program are composed of 85% anhydrite and 15% clay and were hydrostatically-formed under 100 MPa. Results from triaxial tests show that these clay-sulfate rocks have a normalized undrained shear strength of about 0.504-0.792 and a friction angle of 17.2°. The strength of this material is low compared to naturally-occurring shales such as Opalinus shale, which for OCR=14 exhibits normalized shear strength ranging from 2.0-2.5 (Aristorenas,1992). More importantly, these specimens exhibit unusually low strength compared to other naturally-occurring shales of the same OCR. Unlike clayey shales, the overconsolidation of these clay-sulfate specimens is not fully locked in and, therefore, does not appear as increase in strength, as expected by clay models such as SHANSEP. Since these specimens are predominantly anhydrite, it is possible that they do not exhibit the same mechanical behavior as clay shales and thus cannot be described by a model as SHANSEP.

Results from triaxial compression tests also indicate a correlation between the stress-strain behavior and strain rate; specimens sheared at higher strain rates fail at higher axial strain and, in some cases, with higher peak strength. Also, the stress-strain data suggest a possible correlation between stress-strain behavior and confining stress. Since the range of confining stresses used in this testing program is only 20 ksc, the differences in stress-strain curves is subtle. Nevertheless, the data does show that higher confining stresses tend to result in lower peak normalized strength. To confirm this relationship, more tests covering a wider range of confining stresses should be performed.

The specimens fail in a brittle mode at high strain rates and in a ductile mode at low strain rates, for a constant confining stress. Results from two drained tests suggest that higher confining pressures may also cause ductile behavior. Since such a correlation regarding confining pressures is not apparent in the undrained tests, more testing is necessary to assess the validity of this correlation.

Water contents were used to measure the extent of gypsification. Results show evidence of shear-induced gypsification. Due to the intensity of shearing that cause cracking, shear specimens have higher gypsification levels than unsheared samples. Furthermore, there is enhanced, shear-induced gypsification in the shear zone of brittle specimens, which is attributed to dilation. The negative pore pressures due to dilation draws water into the shear zone, which exposes more anhydrite surfaces to water and produces more gypsum. Enhanced gypsification in the shear zone is only observed in specimens that fail brittlely with a shear plane. For specimens that are sheared but fail with bulging, the gypsification levels are more uniform throughout and generally lower than specimens that fail with a shear plane.

From the results of this testing program, it can be concluded that the large swelling of clay-sulfate rock due to gypsification is of concern when the material shears in a brittle mode and forms shear planes. The triaxial tests indicate that the material is likely to fail brittly when sheared at high strain rates and possibly at low confining stresses.

In future work, additional triaxial tests need to be performed to attain full understanding of the behavior of clay-sulfate rocks in the field. Stress paths that simulate field conditions should be used in these tests. Also, relaxation and creep tests should be performed. Specifically, at the peak of the stress-strain curve, the deformation or stress is held constant for a few days before shearing continues. Creep tests would show whether strength decreases with time. To investigate the behavior of clay-sulfate rock in repositories, de-ionized water should be replaced with other pore fluids that simulate the ionic content of leachates in repositories. From such tests, one could assess the effect of pore fluid on the strength and swelling of clay-sulfate rock.

The procedures used in this testing program should also be repeated for clay-sulfate rocks of different compositions. The 85% anhydrite/15% clay material was used in this testing program, because this composition has shown maximum swelling in a previous work (Madsen & Nüesch, 1991). Different compositions may affect the swelling behavior by altering the ability of clay to “bring” water to the anhydrite. Thus, materials of different composition may also result in different gypsification patterns. Lastly, it would be interesting to investigate the possible correlation between gypsification and strength. In isolation, anhydrite has higher strength than gypsum (Zanbak, 1986). Thus, conditions that enhance gypsification may decrease the strength of clay-sulfate rock.



## 5 References

- Aristorenas, G., Time Dependent Behavior of Tunnels Built in Shale, Ph.D. Thesis, MIT, 1992.
- Bellwald, P., A Contribution to the Design of Tunnels in Argillaceous Rocks, Sc.D Thesis, MIT, 1990.
- Bjerrum, L., Simmons, N.E., Comparison of Shear Strength Characteristic of Normally Consolidated Clays, *Proceedings of the 1<sup>th</sup> PSC*, pp.711-726, 1960.
- Brace, W.F., Permeability of Crystalline and Argillaceous Rocks, *International Journal of Rock Mechanics and Mining Sciences, Geomechanics Abstracts*, vol. 17, no. 5, pp.241-251, 1980.
- Gutierrez, M., Vik, G., Berre, T., Shale Strength as Function of Stress History and Diagenesis, *Eurock '96*, ed. Barla, A.A. Balkema, Rotterdam, pp. 69-76, 1996.
- Hardie, L.A., The Gypsum-Anhydrite Equilibrium at One Atmosphere Pressure, *American Mineralogist*, vol. 52, pp.171-200, 1967.
- Jones, M.E., Addis, M.A., On Changes in Porosity and Volume During Burial of Argillaceous Sediments, *Marine and Petroleum Geology*, vol. 2, no. 3, pp.247-253, 1985.
- Jordan, P., Nüesch, R., Deformational Behavior of Shale Interlayers in Evaoprte Detachment Horizons, Jura Overthrust, Switzerland, *Journal of Structural Geology*, vol. 11, no. 7, pp.859-871, 1989.
- Ladd, C.C., Foott, R., New Design Procedure for Stability of Soft Clays, *Journal of Geotechnical Engineering Division*, vol. 100, no. GT4, pp.763-779, 1977.
- Lambe, W.T., Whitman, R.V., *Soil Mechanics*, Wiley & Sons, New York, pp.54-55, 1969.
- Madsen, F.T., Nüesch, R., Characteristics and Sealing Effect of Bentonites, *Geosynthetic Clay Liners: Proceedings of an International Symposium*, ed. Koerner, Gartung, and Zanzinger, A.A. Balkema, Rotterdam, pp.31-49, 1994.
- Madsen, F.T., Nüesch, R., The Swelling Behaviour of Clay-Sulfate Rocks, *Proceedings of the 7<sup>th</sup> International Congress of the International Society for Rock Mechanics*, ed. Wittke, W., Aachen, vol. 1, pp.285-288, 1991.
- McKown, A.F., and Ladd, C.C., Effects of Cementation on the Compressibility of Pierre Shale, *ASTM Special Technical Publication: Geotechnical Properties, Behavior and Performance of Calcareous Soils*, ed. Demars and Chaney, Philadelphia, pp.320-339, 1982.
- Nüesch, R., Ko, S.C., Advantages of Shaley Evaporites as Host Rocks for Underground Waste Storage, *Proceedings of Geotechnika 97* (in press).

Nüesch, R., Madsen, F.T., Steiner, W., Long Time Swelling of Anhydritic Rocks: Mineralogical and Microstructural Evaluation, *Proceedings of the 8<sup>th</sup> International Congress of the International Society for Rock Mechanics*, ed. Fujii, T., Tokyo, vol. 1, pp.133-138, 1995.

Posnjak, E., The System  $\text{CaSO}_4\text{-H}_2\text{O}$ , *American Journal of Science*, ser. 5, vol. 35A, pp.247-272, 1938.

Sheahan, T.C., An Experimental Study of the Time-Dependent Undrained Shear Behavior of Resedimented Clay Using Automated Stress Path Triaxial Equipment, Sc.D Thesis, MIT, 1991.

Zanbak, C., Arthur, R.C., Geochemical and Engineering Aspects of Anhydrite/Gypsum Phase Transitions, *Bulletin of the Association of Engineering Geologists*, vol. 23, no. 4, pp.419-433, 1986.

5/4/5